Targeting ferroptosis and oxidative stress: Ipomoea pes-caprae-synthesized selenium nanoparticles accelerate healing in infected wounds via Nrf2/HO-1 activation.

NEGM, Walaa A, ELEKHNAWY, Engy <http://orcid.org/0000-0001-8287-1026>, HABIB, Doaa A, EL-MASRY, Soha M <http://orcid.org/0000-0002-3437-2713>, ELBEDAIWY, Heba M <http://orcid.org/0000-0002-7406-7481>, ABO-SAIF, Mariam Ali, OMARA, Walid <http://orcid.org/0009-0009-6034-1505>, AL-ASHMAWY, Ghada M, ABDEL-ALL, Sherif R and EL AFIFY, Sherin Refat

Targeting Ferroptosis and Oxidative Stress: *Ipomoea pes-caprae*-Synthesized Selenium Nanoparticles Accelerate Healing in Infected Wounds via Nrf2/HO-1 Activation

Walaa A. Negm [1,†], Engy Elekhnawy [2, †], Doaa A. Habib [3,4], Soha M. El-masry [3], Heba M. ElBedaiwy [3], Mariam Ali Abo-Saif [5], Walid Omara [6], Ghada M. Al-Ashmawy [5,7], Sherif R. Abdel-All [8], Sherin Refat El Afify [9]

[1] Department of Pharmacognosy, Faculty of Pharmacy, Tanta University, Tanta 31527, Egypt.
[2] Microbiology and Immunology Department, Faculty of Pharmacy, Tanta University, Tanta 31527, Egypt.
[3] Department of Pharmaceutics, Faculty of Pharmacy, Damanhour University, P.O. Box 22511, Damanhour, Egypt
[4] Department of Pharmaceutics and Pharmaceutical Technology, Faculty of Pharmacy, Alsalam University, Kafr Alzayat, Algharbia 31611, Egypt
[5] Department of Biochemistry, Faculty of Pharmacy, Tanta University, Tanta 31527, Egypt
[6] Department of Biosciences and Chemistry, Sheffield Hallam University, UK
[7] Department of Biochemistry, Faculty of Pharmacy, Alsalam University, Kafr alzayat, Algharbia 31611, Egypt
[8] Department of Pharmacognosy, Faculty of Pharmacy, Alsalam University, Kafr Al Zayat, Al Gharbia, 31611, Egypt
[9] Department of Pharmacology and Toxicology, Faculty of Pharmacy, Alsalam University, Kafr Alzayat, Algharbia 31611, Egypt

† Authors who have contributed equally
*** Correspondence:** engy.ali@pharm.tanta.edu.eg (E.E)

Abstract

This study was designed to uncover the therapeutic potential of *Ipomoea pes-caprae* extract (IPE) and its green-synthesized selenium nanoparticles (Se NPs) in enhancing the healing of *Pseudomonas aeruginosa*-infected wounds in rats, with a focus on the modulation of ferroptosis and the Nrf2/HO-1 signaling pathway. The HPLC analysis of IPE revealed 14 phenolic acids and flavonoid compounds. The green-synthesized Se NPs were characterized using UV–Vis spectroscopy with peaks at 233 and 277 nm, confirming nanoparticle formation. The XRD indicated a nanocrystalline structure with an average crystallite size of 68.43 nm. The FTIR identified functional groups from the IPE involved in capping and stabilizing the Se NPs. The SEM and TEM images showed predominantly spherical particles, while EDX confirmed elemental selenium alongside carbon and oxygen, indicating phytochemical-mediated synthesis. The DLS

measured a hydrodynamic size of 273.76 ± 0.31 nm with a low polydispersity index (0.202 ± 0.014). Also, the zeta potential analysis showed a value of –26.42 ± 0.35 mV, suggesting strong colloidal stability. These results validate the successful green synthesis of stable and nanoscale Se NPs using IPE. An *in vivo* infected wound model was triggered in rats. Colorimetric, ELISA, and qRT-PCR methods to measure different biochemical markers. It was found that the Se NPs upregulated the expression of GPX4, ferritin, and HO-1, while downregulating PTGS2 and ACSL4, indicating effective suppression of ferroptosis. Immunohistochemical analysis demonstrated enhanced Nrf2 and Ki-67 expression in the Se NPs-treated group, suggesting improved antioxidant activity and cellular proliferation. A computational network pharmacology analysis was also performed, and it revealed that the phytochemicals in IPE considerably enhanced wound healing, lessened oxidative stress, and modulated ferroptosis-related markers. In conclusion, the biosynthesized Se NPs exhibited superior wound healing potential via its antioxidant, anti-inflammatory, antimicrobial, and anti-ferroptotic mechanisms.

Introduction

Wound healing is a multifaceted and dynamic procedure encompassing hemostasis, inflammation, proliferation, and tissue remodeling. A precise balance among these phases is mandatory for successful wound healing. However, certain factors, like infections, could hinder tissue regeneration and predispose to poor closure of the wound, leading to chronic, non-healing wounds. Recent research has underscored the part of ferroptosis, an iron-dependent form of regulated cell death, in hindering the wound healing process (Li et al., 2007). Ferroptosis is a distinct kind of regulated cell death characterized by the presence of iron-dependent lipid peroxides within cells, attributed to factors, such as the inactivation of glutathione peroxidase 4 (GPX4), a key regulator of ferroptosis, and a reduction in the concentration of the antioxidant glutathione (GSH), the primary substrate of GPX4. Ferroptosis can be described as an imbalance between oxidant and antioxidant systems, triggering lipid peroxidation, membrane damage, and cell death. Modulation of ferroptosis-related markers may present a novel therapeutic target for enhancing wound repair (Forcina and Dixon, 2019).

The accumulation of the products of lipid peroxidation within cells is critical to the ferroptosis process. Polyunsaturated fatty acids (PUFAs) are considered the primary substrates of lipid peroxidation and have a vital part in regulating cellular growth, immunity, and inflammation. Free PUFAs are conjugated to CoA by acyl-CoA synthetase long-chain family member 4 (Acsl4) and

subsequently incorporated into membrane phospholipid bilayers via lysophosphatidylcholine acyltransferase 3 (LPCAT3). Lysophospholipids serve as substrates for prostaglandin-endoperoxide synthase 2 (PTGS2), a crucial biomarker for the ferroptosis pathway (Cui et al., 2023).

There is a growing mandate for innovative strategies that might help in the wound healing process. In recent years, nanotechnology has gained noteworthy momentum and has huge promise for a wide range of medical applications, including wound healing. Nanoparticles (NPs) are utilized in pharmaceutical formulations to enhance therapeutic efficacy, improve bioavailability, and mitigate adverse effects. Their diminutive size and modifiable surfaces facilitate targeted drug delivery, controlled release, and improved solubility. Furthermore, nanoparticles support various administration routes, enhance drug stability, and increase the therapeutic index by maximizing efficacy while minimizing side effects (Marles et al., 2011). There are many techniques for the synthesis of NPs, including physical, chemical, and green synthesis. Green synthesis has great advantages over other methods, like safety and affordability (Altammar, 2023).

Ipomoea pes-caprae, commonly or beach morning glory, is a halophytic plant traditionally employed in various medicinal practices (Akinniyi et al., 2022). It has analgesic, anti-inflammatory, and wound-healing effects. Traditionally, *I. pes-caprae* has been utilized to manage various disorders, like intestinal illnesses, skin diseases, and inflammation (Akinniyi et al., 2022). We aimed to investigate the therapeutic action of *Ipomoea pes-caprae* extract (IPE) and its green-synthesized selenium NPs (Se NPs) in promoting the healing of *Pseudomonas aeruginosa*-infected wounds in rats, focusing on the modulation of ferroptosis and the Nrf2/HO-1 signaling. Additionally, a computational network pharmacology will be performed to recognize the bioactive compounds in the IPE and their potential targets and pathways linked to wound healing. Figure 1 reveals a diagrammatic presentation of the various steps performed in this study.

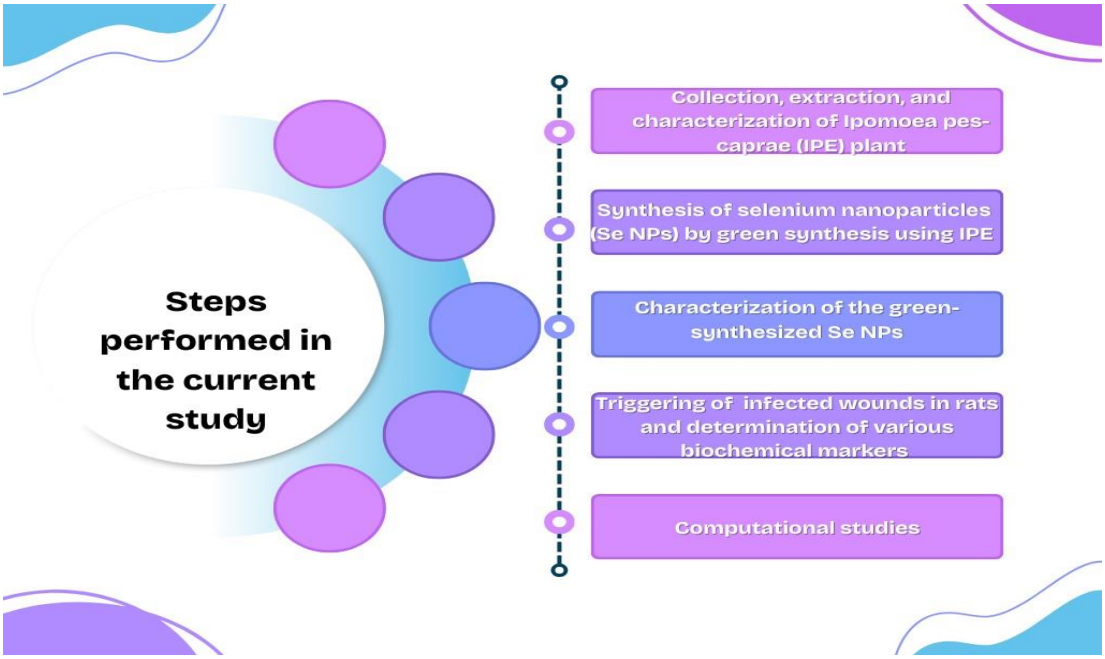

Figure 1. A schematic presentation of the performed steps in the current study.

Material and methods

Plant

Leaves were gathered from a private nursery in Menuofia governorate in October 2024. Dr. Esraa Ammar, Plant Ecology, Tanta University, recognized the plant species. A voucher sample (PG-A-201-W-S) was deposited at the Herbarium of the Faculty, Tanta University.

High performance liquid chromatography (HPLC)

In the supplementary material.

Green synthesis of Se NPs

Nanoparticle synthesis was achieved by mixing the IPE with a selenium precursor salt (1mM sodium selenite solution and while heating at 50°C for 48h. The reaction mixture was perceived for color change and analyzed with a UV–Vis spectrophotometer. After completion of the reaction, the synthesized Se NPs were gathered by centrifugation (Perumal et al., 2021; Ramamurthy et al., 2013).

***In vitro* characterization of Se NPs**

The UV-visible (UV-Vis) spectroscopy and Fourier transform mid-infrared (FTIR) confirmed the successful synthesis of Se NPs by detecting characteristic peaks. X-ray powder diffraction (XRD) analysis revealed the nature and phase purity of the synthesized Se NPs. Dynamic light scattering (DLS) was used to explore the hydrodynamic size, distribution, and surface charge of the Se NPs.

Scanning (SEM)/transmission (TEM) electron microscopy provided insights into the Se NPs' morphology and the particle size distribution. Energy dispersive X-ray (EDX) analysis established the elemental composition of Se NPs. The details of the methods of characterization are listed in the supplementary file.

Animals

The *in vivo* method was performed according to the rules of the use of laboratory animals of the Research Ethical Committee, Faculty of Pharmacy, Alsalam University, Egypt (SUEP/REC/02/25/07/007). Thirty-five male Wistar rats with a body weight of 220-250 g and an age of two months were purchased from the National Research Center (Cairo, Egypt). Animals were fed on pellet chow (El Nasr Chemical®, Cairo, Egypt) and allowed free access to water and nutrients under controlled environmental conditions. The rats were maintained for one week as an acclimatization period.

After the acclimatization, the animals were divided randomly into five groups (n=7) as follows:

- Negative control group (normal rats)
- Positive control group (rats with infected wounds and treated with a vehicle)
- Povidone-iodine treated group (rats with infected wounds and treated with gel preparation containing 10% povidone-iodine)
- IPE-treated group (rats with infected wounds and treated with IPE)
- Se NPs-treated group (rats with infected wounds and treated with Se NPs)

All treatments were applied daily for 15 days on the injury area using a sterile bandage. For wound generation, the animals were anesthetized, and then the hair on the dorsal area was shaved. After hair removal, a circular full-thickness dermal cut (1×1 cm) was generated by the surgical blades (Zhu et al., 2019). For a generation of infected wounds, *Pseudomonas aeruginosa* (PAO1) suspension was applied to cover the wound immediately after wound generation. On postoperative days (0, 3, 6, 9, 12, and 15), the wounded area of the skin was imaged by a digital camera, and the surface area of the wound was calculated by multiplying the highest length of the wound by the perpendicular highest width. The highest length and width of the wounded area were determined using a ruler (Negm et al., 2022). After 15 days, animals were decapitated, and the wounded skin was collected for further assessment. Further biochemical and histological investigations were performed (supplementary file).

Computational studies (supplementary file)

Statistics

Using the software Graph Pad prism, our collected data were subjected to one-way ANOVA analysis for statistical comparison between different groups, followed by post-hoc Fisher's least significant difference (LSD). The $p<0.05$ was statistically significant.

Results

HPLC

HPLC of IPE exposed the incidence of phenolic acids, like gallic acid, chlorogenic acid, syringic acid, ellagic acid, coumaric acid, ferulic acid, and rosmarinic acid, flavonoids, like rutin, naringenin, daidzein, quercetin, catechin, and miscellaneous compounds, like methyl gallate and vanillin. It was found that the rutin is the major flavonoid compound identified (164.86 µg/g dry wt.), followed by gallic acid as the main phenolic acid identified (98.94 µg/g dry wt.) Figure 2 and Table S1.

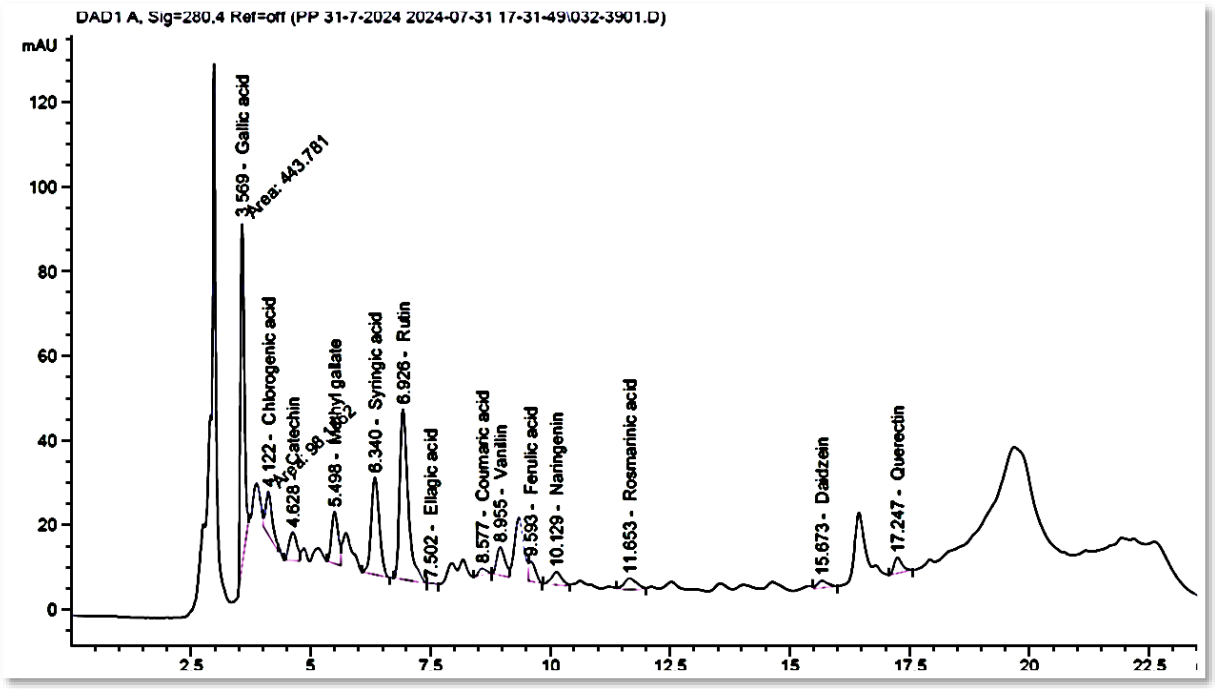

Figure 2. The HPLC chromatogram of the *Ipomoea pes-caprae* leaves

Characterization of the Se NPs

UV-Vis spectroscopy

The UV-Vis spectrum of IPE and Se NPs is displayed in Figure 3A. The absorption peaks of IPE are at 231, 271, 314 and 658 nm while Se NPs revealed maximum absorption peaks at 233 and 277 nm.

FTIR spectroscopy

FTIR analysis was employed to elucidate the functional groups that are related to the interaction between IPE and Se NPs during the synthesis process. Additionally, FTIR analysis was accomplished to recognize the functional groups present in the IPE. As shown in Figure 3B, the presence of alcohol moieties is indicated by a spectral peak at 3403.78 cm^{-1}, signifying the OH bond within IPE, demonstrating the existence of phenolic compounds. The peak at 3266.84 cm^{-1} reflects N-H stretch, suggesting the existence of alkaloids in the IPE. The existence of the C-H stretching vibration at 2942.16 cm^{-1} and 2854.65 cm^{-1} indicates the presence of CH_2 and CH_3 groups, suggesting the presence of terpenes. Additionally, the absorption peaks at 1717.22 cm^{-1} and 1605.70 cm^{-1} suggest the presence of N-O asymmetrical stretch, and C-C stretching in the IPE. The peaks at 1209.50 cm^{-1} and 1356.27 cm^{-1} support the C-N stretching, C-H and C-O blend. The observed absorption bands at 1074.85 cm^{-1} and 1018.61 cm^{-1} are indicative of C-O stretching vibrations, arising from ester or secondary alcohol groups. Peaks at 529.87 cm^{-1} reflected the C-N-C Stretching. The existence of these peaks suggests the presence of alkaloids, flavonoids, terpenes, and phenolic compounds within the IPE.

Regarding the FTIR analysis of the Se NPs (Figure 3B), a broad peak is observed at 3411 cm^{-1} corresponding to O–H stretching. The absorption peaks at 2938 cm^{-1} and 2977 cm^{-1} correspond to the C-H stretch. The strong band at 1644 cm^{-1} is due to C-C stretching. Also, the bands at 1571 cm^{-1} and 1375 cm^{-1} indicate N-O stretch and C-H bending, respectively. The peaks at 1077 cm^{-1}, 1044 cm^{-1}, and 1012 cm^{-1} correspond to the C–N stretching.

XRD of Se NPs

It was implemented to explore the crystalline behavior of the synthesized Se NPs (Figure 3C). The amorphous nature of the Se NPs was initially revealed. However, some Bragg reflections with 2θ values at 11.6083º, 22.122º, and 34.4468º were observed. The crystallite size of the Se NPs was calculated using the Scherrer equation with an average size of 68.43 nm.

Particle size, PDI, and zeta potential of Se NPs

DLS analysis confirmed the homogeneous dispersion of the Se NPs with an average size of 273.76 ± 0.305 nm and a PDI of 0.202 ± 0.014 (Figure 3D). The Se NPs exhibited a high negative zeta potential of -26.42 ±0.351 mV (Figure 3E).

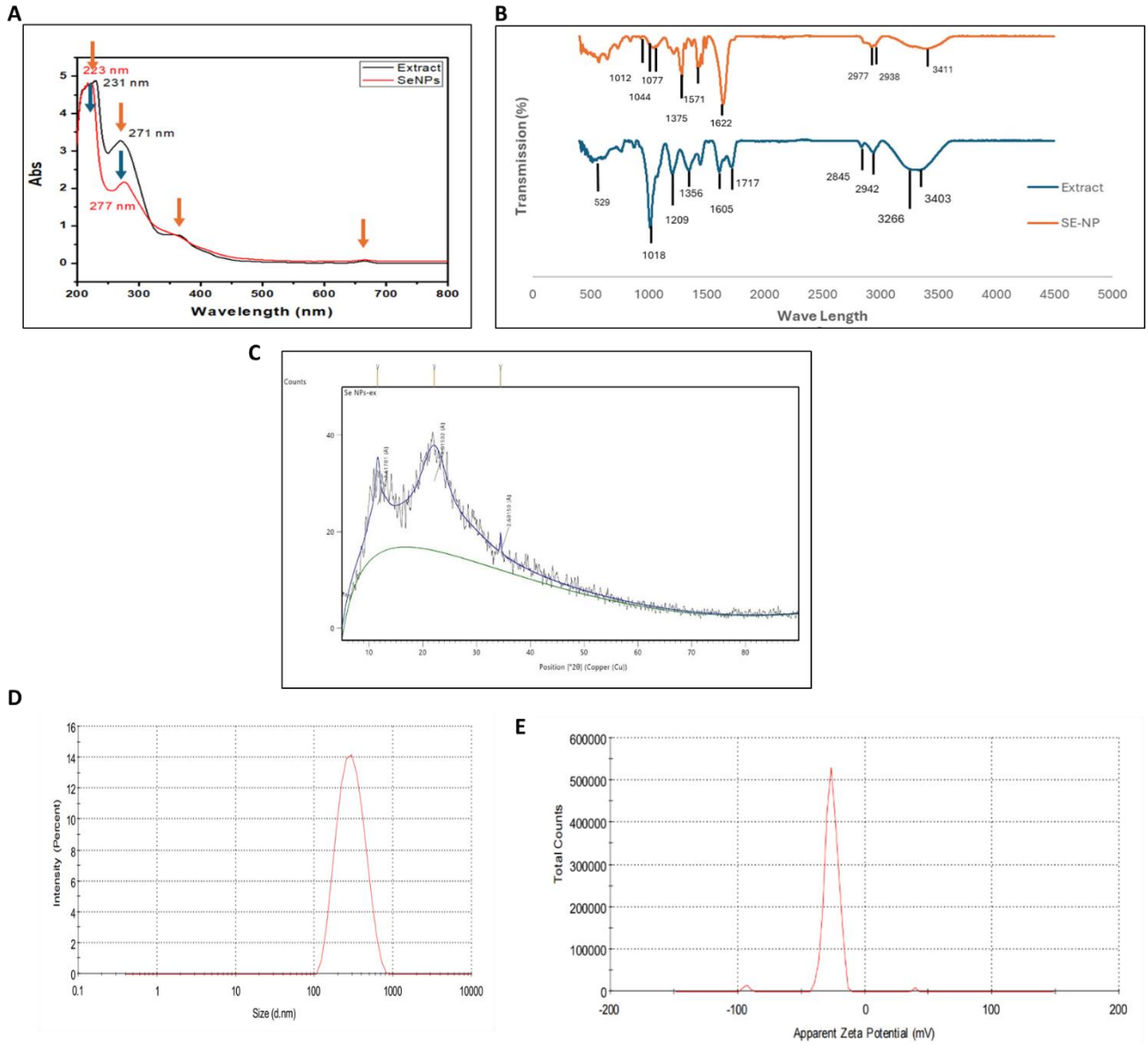

Figure 3. A) The UV-Vis spectra of *Ipomoea pes-caprae* extract and the Se NPs. B) The FTIR spectra of *Ipomoea pes-caprae* extract and the Se NPs. C) The XRD pattern of Se NPs. D) Dynamic light scattering analysis of Se NPs. E) Zeta potential of Se NPs.

SEM, TEM, and EDX

SEM micrograph of the Se NPs displayed spherical particles with slightly irregular surface (Figure 4A). The TEM micrograph exposed a spherical structure of Se NPs with an average particle diameter of 70 ±10 nm (Figure 4B).

The EDX analysis reveals the elemental composition of the synthesized Se NPs, predominantly consisting of carbon (75.32%) and oxygen (19.33%) (Figures 4C and 4D). In addition, selenium (2.71%) was also detected, confirming its incorporation into the sample. This suggests a successful synthesis of the Se NPs. The existence of carbon and oxygen within the Se NPs provides evidence for the green synthesis approach, suggesting the involvement of organic compounds as capping agents for Se-NPs. The presence of trace amounts of sodium (1.54%), chlorine (0.76%), and potassium (0.34%) may be attributed to residual ions from reagents used during the synthesis process. The identifiable peaks in the spectrum confirmed the high purity of the synthesized Se NPs.

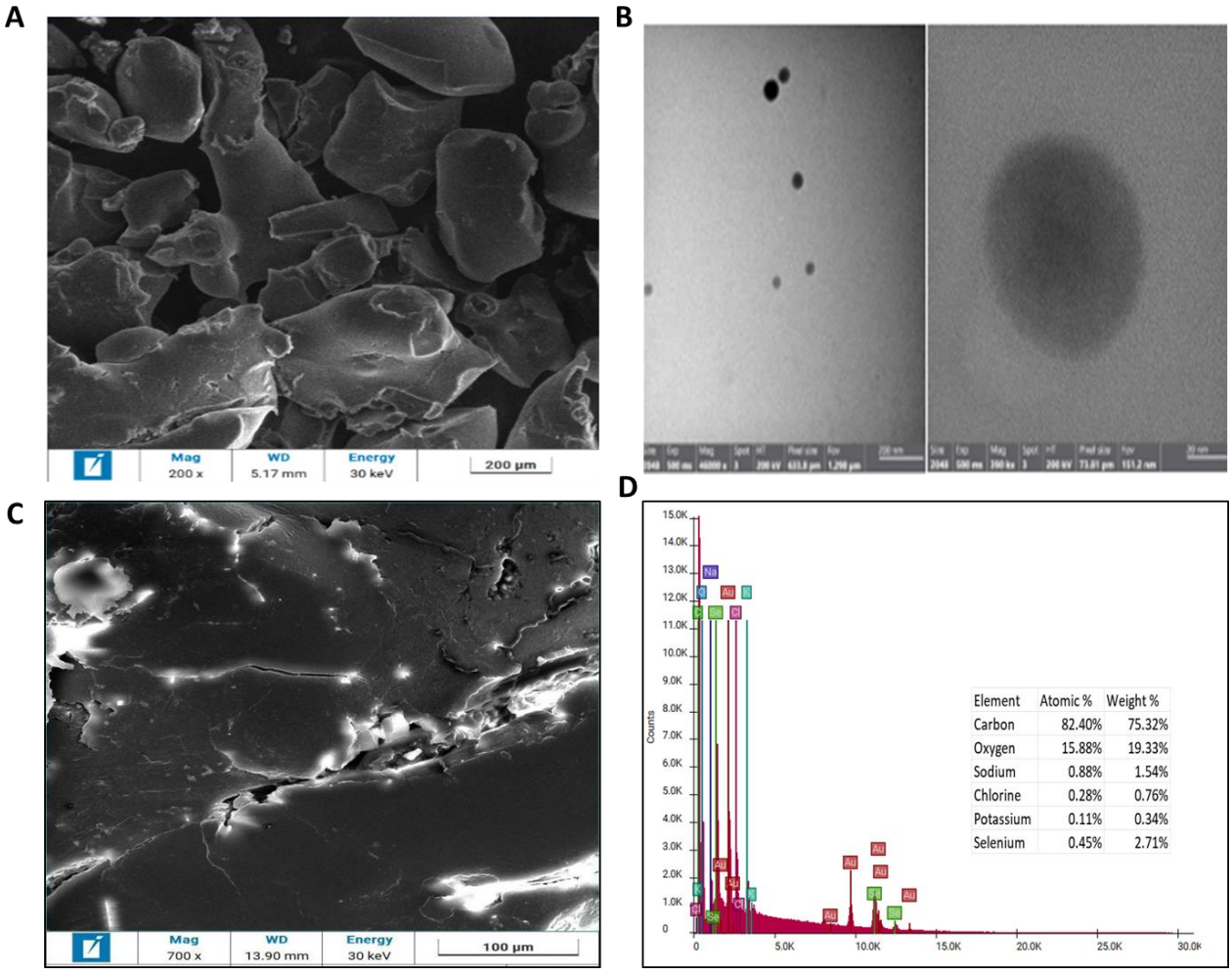

Figure 4. A) Scanning electron micrograph. B) Transmission electron micrograph. C) The EDX of Se NPs. D) Elemental mapping revealing the distribution of Carbon, oxygen, and selenium.

Wound healing potential of SE NPs

Treatment of infected wounds with povidone-iodine and Se NPs displayed a substantial decrease (p<0.05) in the wound area compared to untreated wounds in the positive control group at days 3, 6, 9, 12, and 15 postoperatively. Meanwhile, treatment of infected wounds with IPE presented a noteworthy lessening (p<0.05) in wound area compared to untreated infected wounds in the positive control group at days 9, 12, and 15 postoperatively (Figure 5).

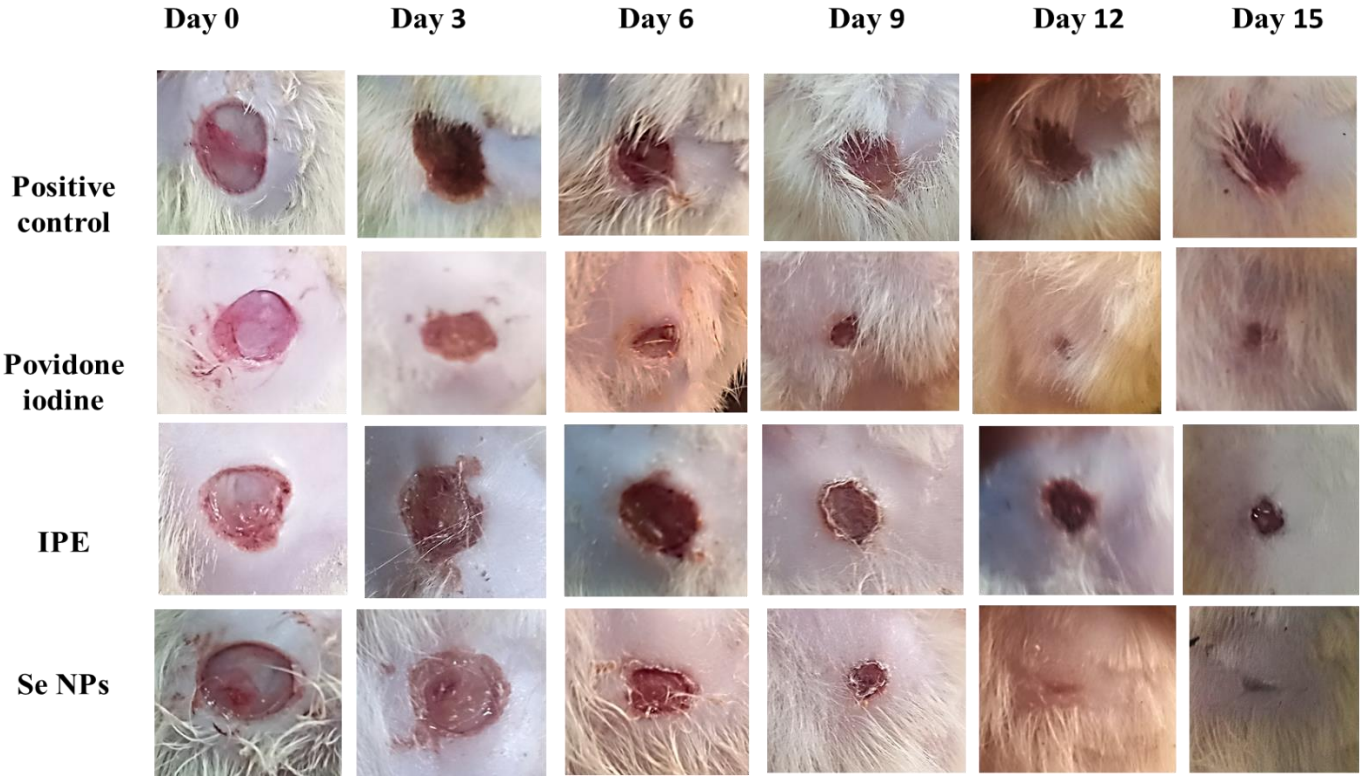

Figure 5. Representative images of the wounded skin in the dorsal side of the studied rat groups at days 0, 3, 6, 9, 12, and 15 after injury. Positive control: infected wound treated with vehicle. Povidone iodine: infected wound treated with povidone iodine. IPE: infected wound treated with *I. pes-caprae* extract. Se NPs: infected wound treated with the Se NPs.

More interestingly, the Se NPs-treated group revealed a substantial lessening (p<0.05) in the wound area compared to the infected wounds treated with povidone-iodine at days 6, 9, and 12 postoperatively. Furthermore, the application of Se NPs and povidone-iodine on the infected wound area ameliorated signs of inflammation and the presence of discharge in the infected wound

area (Figure S1A). Also, the number of colony-forming units per gram tissue (CFU/g) was considerably lessened (p<0.05) in the Se NPs-treated group (Figure S1B).

Colorimetric studies

At the end of our experiment, the level of MDA as a marker of lipid peroxidation and the level of reduced GSH (the main substrate of GPX4) were measured in the tissue homogenate from the injured skin. Induction of injury significantly increased (p<0.05) the MDA and decreased GSH concentrations in the wounded area compared to uninjured skin from the negative control group (p<0.05). Interestingly, the topical application of IPE and Se NPs considerably lessened (p<0.05) the MDA and elevated GSH levels compared to the positive control group (p<0.05). Moreover, the consequence of the Se NPs on regulating the oxidative stress in the wound was considerably greater (p<0.05) when compared to the IPE (p<0.05) (Figures 6A and 6B).

ELISA for assessing the ferritin, glutathione peroxidase 4 (GPX4), and heme oxygenase-1 (HO-1) levels

At the end of our experiment, the anti-inflammatory marker HO-1, as well as ferroptosis-related markers ferritin and GPX4, were measured in the wound tissue homogenate using ELISA technique. Treatment of infected wounds with our different treatments significantly increased (p<0.05) GPX4, ferritin, and HO-1 in the wounded area compared to untreated infected wounds in the positive control group (p<0.05). Furthermore, the concentration of HO-1, GPX4, and ferritin in infected wounds treated with Se NPs was significantly higher than in other studied groups (p<0.05) (Figures 6C to 6E).

The expression of GPX4, prostaglandin-endoperoxide synthase 2 (PTGS2), and acyl-coA synthetase long-chain family member 4 (ACSL4) genes

To confirm the effect of our treatments on the ferroptosis pathway, the gene expression of the ferroptosis-related markers (GPX4, PTGS2, and ACSL4) in the wounded area was assessed using qRT-PCR. Our findings revealed that topical application of our treatments to the infected wound considerably amplified (p<0.05) the gene expression of GPX4, while significantly decreasing (p<0.05) the gene expression of both PTGS2 and ACSL4 in the wounded area compared to the untreated infected wound in the positive control group (p<0.05). More interestingly, the gene expression of the measured ferroptosis-related markers (GPX4, PTGS2 - ACSL4) in the infected wound treated with Se NPs was considerably different from the other studied groups (p<0.05) (Figures 6F to 6H).

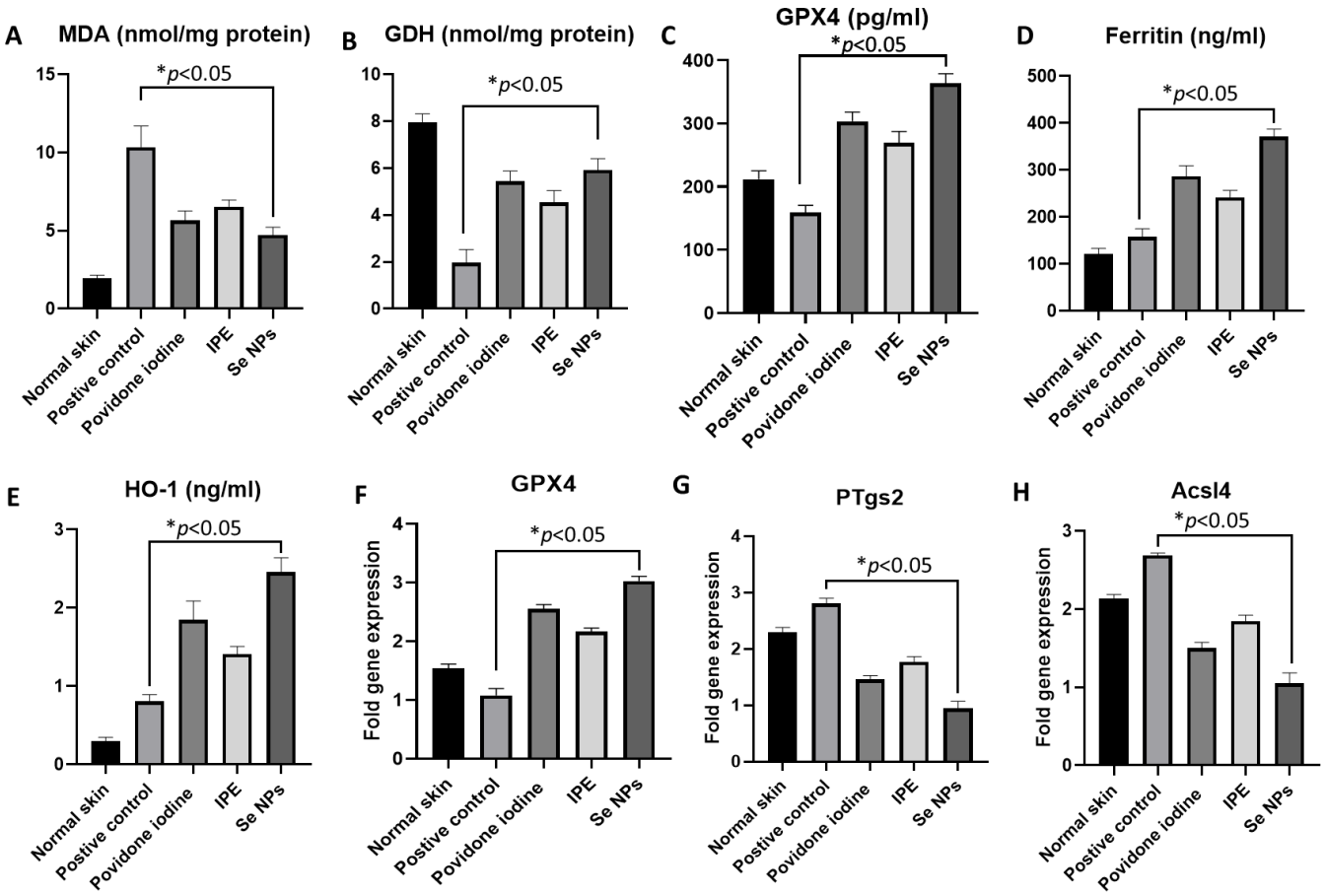

Figure 6. Consequence of different treatments on the concentration of (A) malondialdehyde (MDA), (B) reduced glutathione (GSH), (C) glutathione peroxidase 4 (GPX4), (D) ferritin, and (E) heme-oxygenase 1 (HO-1) as well as gene expression of (F) glutathione peroxidase 4 (GPX4), (G) prostaglandin-endoperoxide synthase 2 (PTGS2), and (H) acyl-CoA synthetase long chain family member 4 (ACSL4). Positive control: infected wound treated with vehicle. Povidone iodine: infected wound treated with povidone iodine. IPE: infected wound treated with IPE. Se NPs: infected wound treated with Se NPs.

Histopathological results

At the end of the current study, the rats were sacrificed, and the skin from the injured area was collected for further histopathological examination. Figure 7 displays the hematoxylin and eosin (H&E)-stained skin section from normal skin in the negative control group with normal epidermis and dermis containing normal sweat glands, sebaceous glands, and hair follicles. On the other hand, wounded skin in the positive control group displayed obvious loss of epidermal layers, which was replaced by heavy polymorphonuclear cell infiltration and granulation tissue filling the wound

gap, composed of young capillary beds, mononuclear cells, and immature fibroblasts. Moreover, wounded skin from rats treated with povidone-iodine showed complete re-epithelization of the new epidermis with an increased amount of vascularized immature connective tissue deposition filling the wound gap. Meanwhile, the wounded skin from rats treated with IPE showed partial re-epithelialization of the new epidermis with granulation tissue filling the wound gap and a small amount of vascularized immature connective tissue deposition. More interestingly, the wounded skin from rats treated with Se NPs shows complete re-epithelialization of the new epidermis with an increased amount of vascularized well-organized, mature connective tissue deposition filling the wound gap (Table S2).

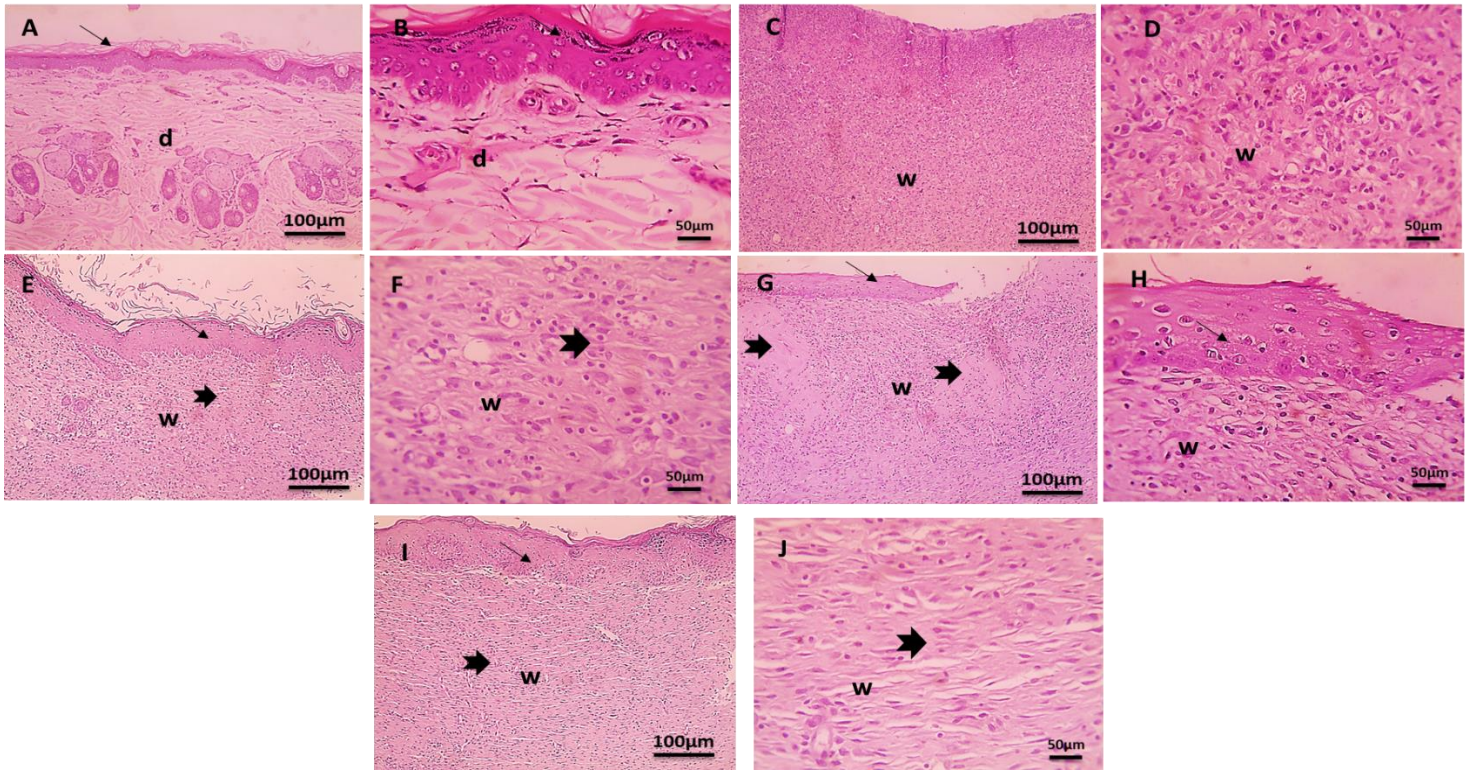

Figure 7. Microscopic images of H&E-stained skin sections. A and B: The normal skin in the negative control group showing normal epidermis (thin arrows) and dermis (d) containing normal sweat glands, sebaceous glands, and hair follicles. C and D: The positive control group showing obvious loss of epidermal layers which replaced by heavy polymorphnuclear cells infiltration and granulation tissue filling the wound gap (w) composed of young capillary beds, mononuclear cells, and immature fibroblasts infiltration. E and F: The povidone iodine-treated group showing completed re-epithelization of new epidermis (thin arrow) with increased amount of vascularized immature connective tissue deposition (thick black arrow) filling wound gap (w). G and H: The

IPE-treated group showing partial re-epithelization of new epidermis (thin arrow) with granulation tissue filling wound gap (w) and little amount of vascularized immature connective tissue deposition (thick black arrow). I and J: The Se NPs-treated group showing completed re-epithelization of new epidermis (thin arrow) with increased amount of vascularized well organized mature connective tissue deposition (thick black arrow) filling wound gap (w). (Magnifications: ×100 bar 100 and ×400 bar 50).

Immunohistochemical results

For further confirmation of the anti-inflammatory properties of our treatments, nuclear factor erythroid 2-related factor 2 (Nrf2) was explored in the wounded area of different groups by using the immunohistochemical method. Figure 8 shows a normal expression for Nrf-2 in the epidermis and dermis of normal skin in the negative control group, while wounded skin from the positive control group shows increased expression for Nrf-2 mainly in the wound gap due to loss of epidermal layers. Furthermore, wounded skin from rats treated with the IPE showed slightly higher expression for Nrf-2 in the epidermis and wound gap, while wounded skin from rats treated with povidone-iodine showed much higher expression for Nrf-2 in the epidermis and wound gap. More interestingly, wounded skin from rats treated with the Se NPs showed the highest expression for Nrf-2 in the epidermis and wound gap. Further, the percentage of immunostaining area was considerably greater in the wounded skin treated with Se NPs compared to other studied groups ($p<0.05$).

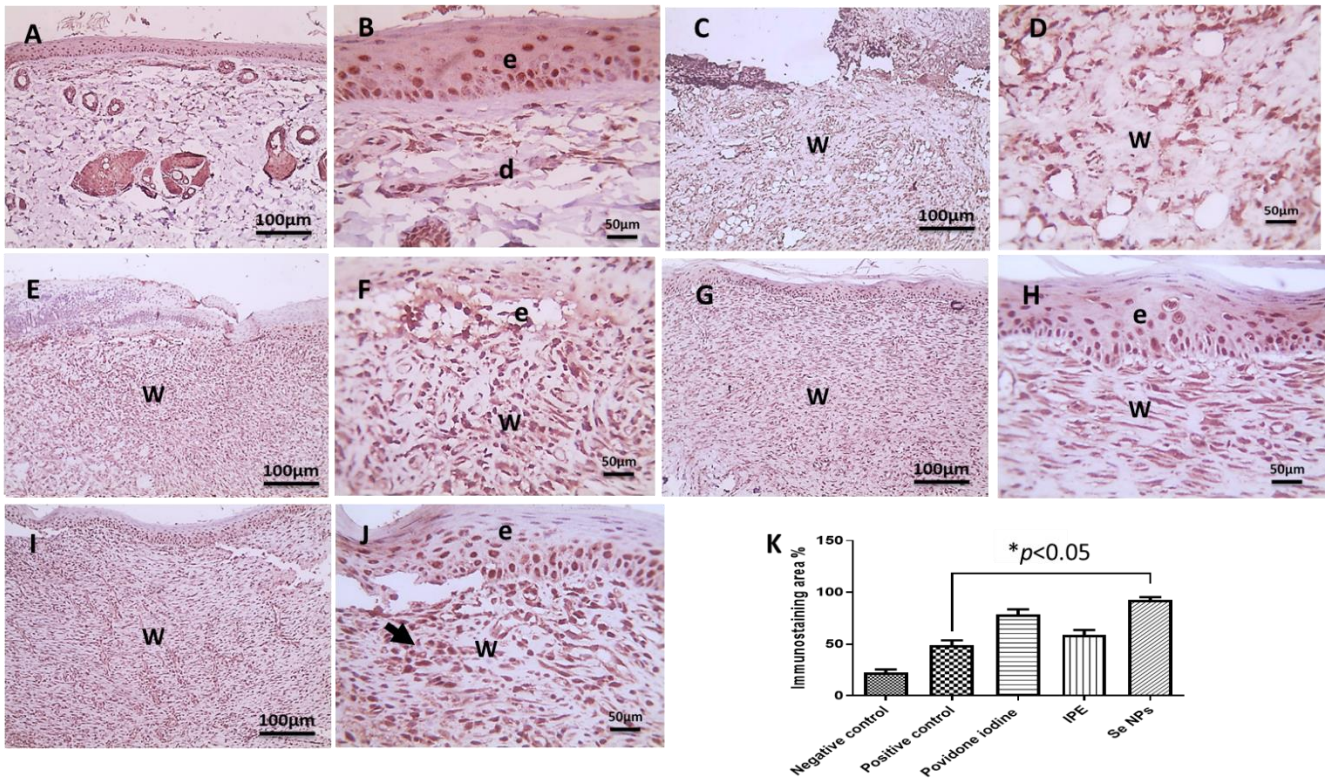

Figure 8. Microscopic images of the immunostained skin sections. A and B: Normal skin in the negative control group showing normal expression for the Nrf-2 in the epidermis (e) and the dermis (d). C and D: Positive control group showing increased expression for Nrf-2, mainly in the wound gap (W) due to loss of epidermal layers. E and F: The IPE-treated group showing slightly higher expression for Nrf-2 in epidermis (e) and wound gap (W). G and H: The povidone iodine-treated group showing much higher expression for Nrf-2 in epidermis (e) and wound gap (W). I and J: Se NPs-treated group showing the highest expression for Nrf-2 in the epidermis (e) and wound gap (W). IHC counterstained with Mayer's hematoxylin. (Magnifications: ×100 bar 100 and x400 bar 50). K: The percent of immunostaining area, the bars demonstrate mean ± SD for Nrf-2 expression levels in skin from all groups.

As a marker of cell proliferation, Ki-67 was determined in the wounded area by the immunohistochemical method (Figure 9), showing normal expression for Ki-67 in the epidermis and dermis of normal skin in the negative control group. On the other hand, wounded skin from the positive control group showed slightly increased expression for Ki-67 in wound gap-staining inflammatory cells, endothelial cells, and fibroblasts. Moreover, wounded skin from rats treated with the IPE showed much augmented the expression of Ki-67 in the wound gap. Further, wounded

skin from rats treated with povidone-iodine showed much higher expression of Ki-67 in the epidermis and wound gap. Meanwhile, wounded skin from rats treated with Se NPs showed the highest expression for Ki-67 in the epidermis and wound gap. Further, the percentage of immunostaining area was considerably greater in wounded skin treated with Se NPs compared to other studied groups (p<0.05).

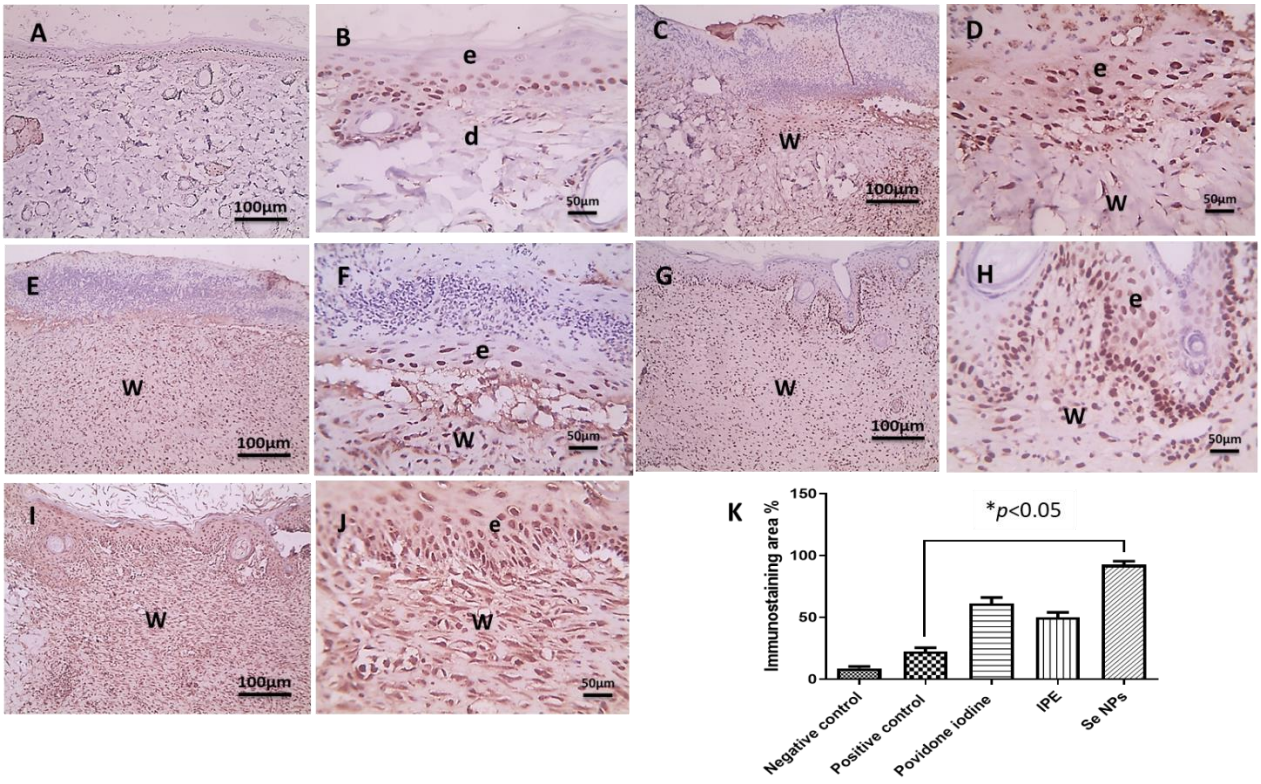

Figure 9. Microscopic images of immunostained skin sections. A and B: Normal skin in the negative control group showing normal expression for Ki-67 in epidermis (e) and dermis (d). C and D: Positive control group shows slightly increased expression for Ki-67 in wound gap (W) staining inflammatory cells, endothelial cells, and fibroblasts. E and F: The IPE-treated group showing much increased expression for Ki-67 in the wound gap (W). G and H: The povidone iodine-treated group showing much higher expression for Ki-67 in epidermis (e) and wound gap (W). I and J: Se NPs-treated group showing the highest expression for Ki-67 in epidermis (e) and wound gap (W). IHC counterstained with Mayer's hematoxylin. (Magnifications: ×100 bar 100 and ×400 bar 50). K: The percent of immunostaining area, the bars demonstrate mean ± SD for Ki-67 expression levels in skin from all groups (n=4).

Computational analysis

Bioactive compounds-target network

The evaluation of the major compounds detected in the IPE, utilizing oral bioavailability (OB) and drug-likeness (DL) metrics, revealed that two bioactive compounds, chlorogenic cid and rutin, are unsuitable for computational study. The exploration of data displayed that 768 catechin targets interacted with coumaric acid 56, 36 targets interacted with daidzin, 159 targets interacted with ellagic acid, 129 targets interacted with ferulic acid, 381 gallic acid targets, targets interacted with methyl gallate 758, 149 targets interacted with naringenin, 840 targets interacted with quercetin, 73 targets interacted with rosmarinic acid, 203 syringic acid targets and 53 interacted with vanillin. The target genes of the 12 bioactive compounds were combined and filtered to eliminate duplicates. Cytoscape 10.2.1 was employed to inspect the interaction between the target genes and the bioactive compounds. The network of the bioactive compounds and target genes had a total of 1587 nodes and 3032 edges. Out of these, 1671 nodes denote the target genes of bioactive compounds. In this network, the degree of a node is determined by the number of connections it has, with nodes having more connections regarded as major bioactive compounds or vital target genes (Figure 10).

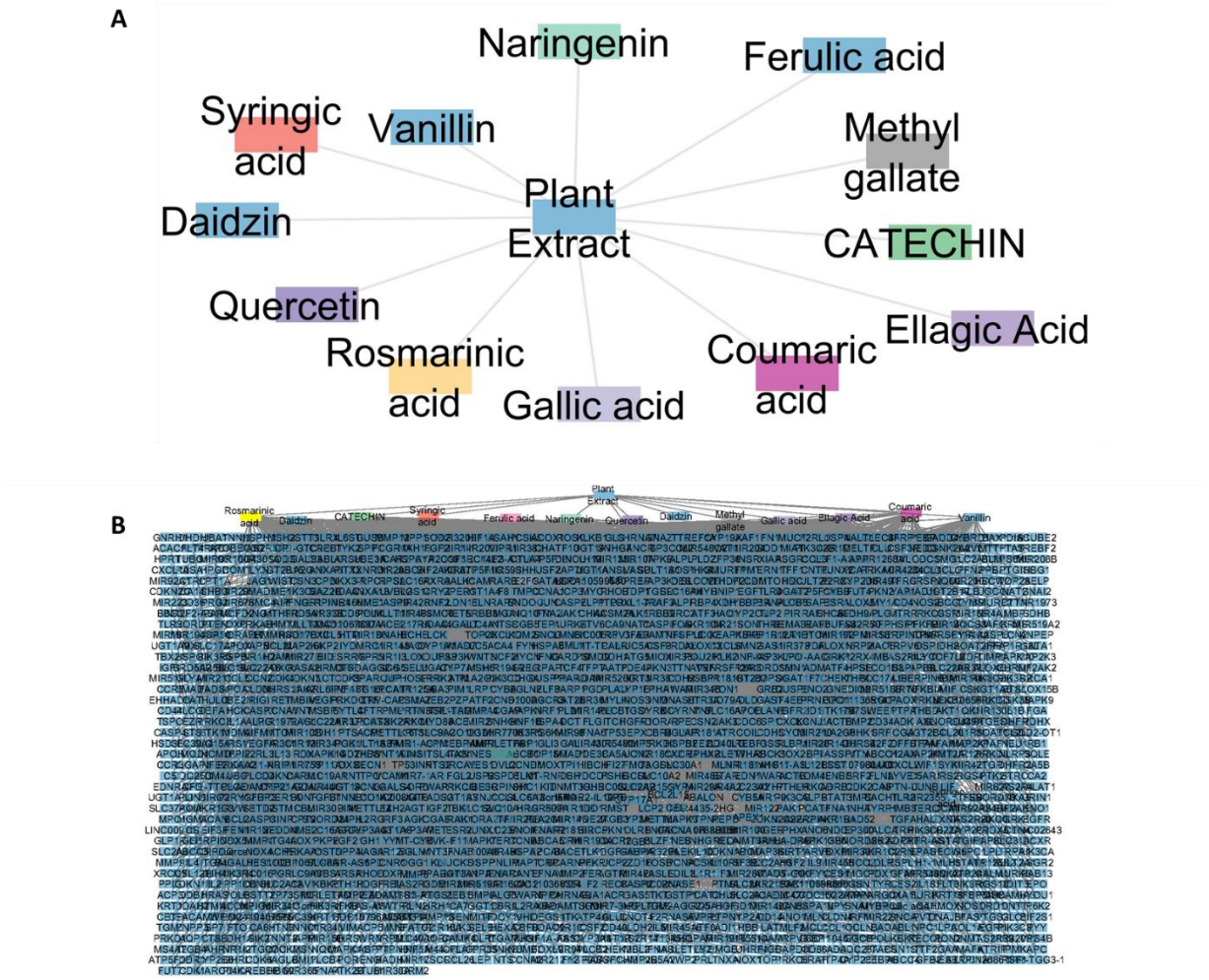

Figure 10. A) The IPE bioactive compounds network. B) Bioactive compound–target network of the bioactive compounds in the IPE. The blue square represents the IPE. Squares of various colors indicate the bioactive compounds; the blue squares represent the targets of the bioactive compounds, identified by their UniProt names. Edges illustrate the interactions between bioactive compounds and their targets.

Target screening of infected wound healing

The keyword " infected wound healing " was selected in the human gene database (GeneCards) to recognize infected wound healing targets, yielding 6473 targets. Consequently, human gene names were updated using the UniProt database. The common target genes among bioactive compounds and infected wound healing were then recognized via the intersection of their obtained targets, and a Venn diagram was established. A total of 1226 shared targets were recognized (Figure 11A).

Protein-protein interaction (PPI) network

The interaction among the 1226 potential therapeutic targets was explored using the STRING database. The obtained PPI network comprised three clusters with 1062 nodes and 47783 edges, with an average node degree of 90 and an average clustering coefficient of 0.476. The PPI enrichment *p*-value is < 1.0e-16. Each node in the network denotes a target protein, and each edge represents a PPI.

The greater the node degree value, the more pivotal the protein's role in the network. In cluster 1 average node degree is 90.5, in cluster 2, the average node degree is 7.45, and in cluster 3 average node degree is 4.57 (Figure 11B). The degree of nodes was evaluated by a Cytoscape plugin known as CytoHubba, which affords an accessible platform for network analysis with various scoring techniques. The utilized one in our study was the maximal clique centrality method (MCC) (Table S3).

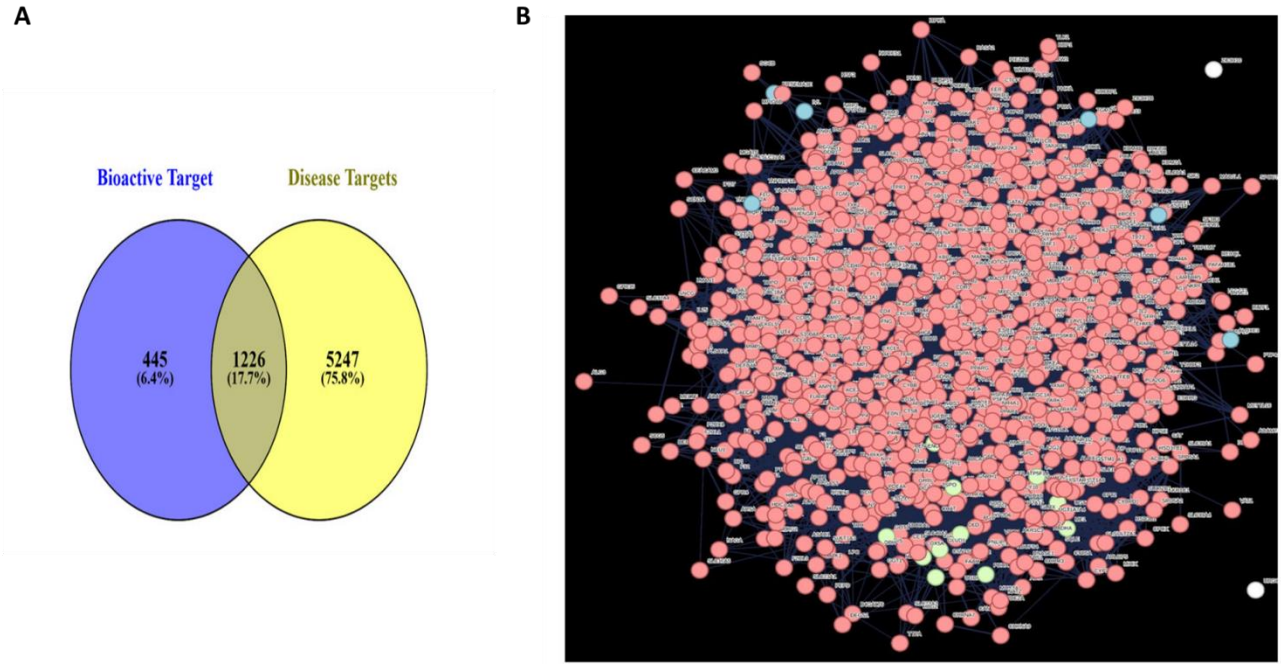

Figure 11. A) The Venn diagram demonstrates the shared target genes between bioactive compounds of the IPE and those of infected wound healing. The size of the circles relates to the number of target genes, with the blue circle representing bioactive compounds target genes, and the yellow circle indicating target genes associated with infected wound healing. The overlapping region signifies the common. B) STRING network analysis displaying protein-protein interactions. Color nodes represent query proteins and the first shell of interactions. Red, green, and blue colors denote clusters 1, 2, and 3, respectively. The nodes in the network denote individual proteins, while

the edges connecting them signify specific protein-protein associations. The different colors of the nodes indicate varying levels of interaction. The colored nodes denote query proteins and their first shell of interactors, while the white nodes denote the second shell of interactors. Empty nodes signify proteins with unknown three-dimensional structures, whereas filled nodes indicate that the three-dimensional structures are known or predicted. The edges denote both functional protein associations and line thickness, indicating the strength of the interaction.

MCC enables researchers to rank nodes based on their centrality score, thereby facilitating the identification of key nodes that significantly influence the structure and functioning of the network. Our analysis revealed that tumor necrosis factor alpha (TNF-α), interleukin-6 (IL-6), Signal transducer and activator of transcription 3 (STAT3), glyceraldehyde 3-phosphate dehydrogenase (GAPDH), interferon gamma (IFNG), Transforming growth factor beta 1 (TGF-β1), matrix metalloproteinase-9 (MMP9), nuclear factor kappa-beta (NF-kβ), interleukin-1 beta (IL-1β), and interleukin 8 or CXCL8 was a centrally positioned hub gene in the PPI network, implying its potential role in the healing of infected wounds (Figure 12A).

Bioactive compounds–genes–disease network

The pharmacology network was established by integrating the plant-bioactive, bioactive-target, and target-disease networks. This comprehensive pharmacology network elucidates the interconnections among bioactive compounds present in plant extracts, their corresponding target genes, and infected wound healing, as illustrated in Figure 12B.

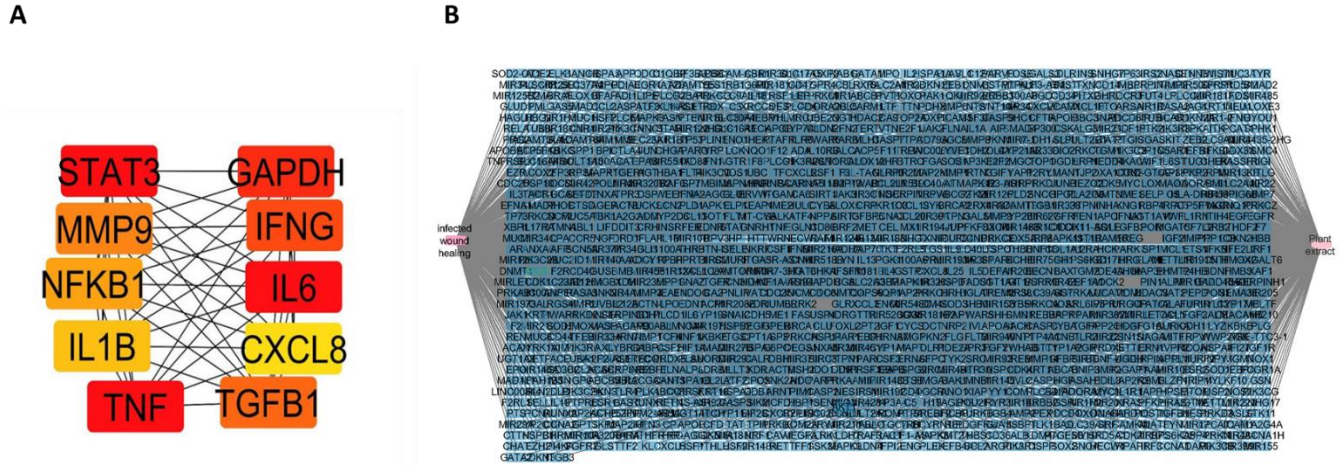

Figure 12. A) Hub genes were identified using the CytoHubba plugin in Cytoscape 3.10.2 by loading a PPI network. The selected nodes are displayed in a color scheme that represents their level of importance, ranging from highly essential (red) to essential (yellow). B) Total merged

networking of the bioactive compounds-targeted gene-targeted disease: the pink octagon represents plant extracts, while blue squares denote uniprot gene names. The pink rectangle represents the disease.

GO enrichment analyses

It was performed on the 1226 potential therapeutic targets in wound healing. Figure 13 visually denotes the top 10 Gene Ontology (GO) terms. In the chart, the length of the lollipop graph corresponds to the number of enriched target genes, while the color gradient from blue to red signifies a decrease in p-values associated with that specific GO term. This implies a stronger association of the identified GO term with infected wound treatment compared to other GO terms.

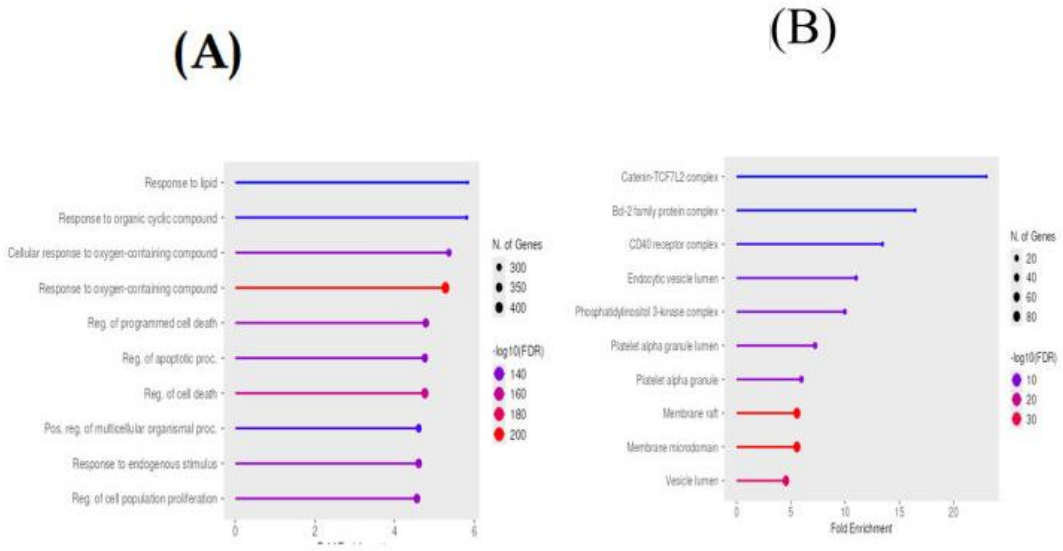

Figure 13. The GO enrichment analysis: A) Biological function and B) Cellular component.

Our analysis highlighted that the principal enriched Biological Process (BP) categories included are response to oxygen-containing compound, Reg of cell death, and Reg of cell population proliferation. The analysis of cellular components (CC) unveiled that the membrane raft, the membrane microdomain, and the vesicle lumen are considered the major enriched cellular component categories involved.

KEGG pathway enrichment analyses

To explore the relationship between bioactive compounds' target genes and infected wound healing, the bioinformatics tool Shinygo (http://bioinformatics.sdstate.edu/go/) was employed to

demonstrate the pertinent biological KEGG pathways based on their enrichment scores. After conducting a comprehensive analysis of 10 signaling pathways with an FDR of less than 0.05 (Figure 14). The results revealed that pathways that are enriched with hub genes are Lipid and atherosclerosis, microRNAs in cancer, Kaposi sarcoma-associated herpesvirus infection, Hepatitis B, and the AGE-RAGE signaling pathway in diabetic complications.

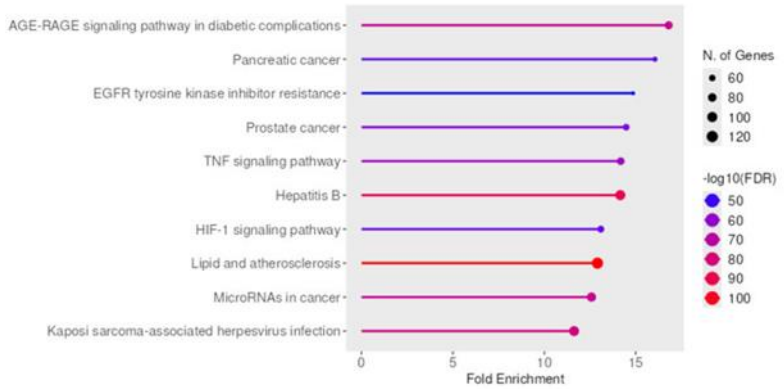

Figure 14. Top 10 significant pathways identified by KEGG pathway enrichment analysis. The names of KEGG signal pathways in which plant extract bioactive compounds target genes are enriched are represented on the ordinate, while the fold enrichment is depicted on the abscissa.

Drug-likeness of bioactive compounds

It was conducted based on the Lipinski's rule of five. This rule specifies that a compound must not exceed one violation in the following criteria: a maximum of five hydrogen bond donors, a maximum of ten hydrogen bond acceptors, a maximum molecular weight of 500 Da, and a maximum octanol-water partition coefficient (log P) of 5 (Table 1).

Table 1. Estimation of the drug-likeness and oral bioavailability.

Bioactive compound	Bioavailability Score	Drug likeness
Gallic acid	0.56	Yes, 0 violation
Chlorogenic acid	0.11	Yes, 1 violation: NHorOH>5
Catechin	0.55	Yes, 0 violation
Methyl gallate	0.55	Yes, 0 violation
Caffeic acid	0.56	Yes, 0 violation
Syringic acid	0.56	Yes, 0 violation
Rutin	0.17	No; 3 violations: MW>500, NorO>10, NHorOH>5
Ellagic acid	0.55	Yes, 0 violation
Coumaric acid	0.85	Yes, 0 violation
Vanillin	0.55	Yes, 0 violation
Ferulic acid	0.85	Yes, 0 violations

Rosmarinic acid	0.56	Yes, 0 violations
Daidzin	0.55	Yes, 0 violations
Quercetin	0.55	Yes, 0 violations
Naringenin	0.55	Yes, 0 violations

Discussion

We aimed to inspect the therapeutic action of IPE and its green-synthesized Se NPs in promoting the healing of *Pseudomonas aeruginosa*-infected wounds in rats. IPE has extensive medicinal applications as it is a rich source of phenolic compounds and flavonoids. It was reported that IPE contains various phytochemical groups like alkaloids, glycosides, steroids, flavonoids, phenols, volatile compounds, and isoprenoids (Chan et al., 2016). We found that rutin is the main active constituent identified in the IPE, which was in accordance with a previous investigation (Kamal et al., 2017). Chlorogenic acid, quercetin, and catechin have been previously identified in IPE and *I. batatas* leaf extract (Sultana et al., 2024; Xavier-Santos et al., 2022), which is found to be in accordance with our results. Here, the HPLC analysis of the IPE revealed 14 bioactive compounds: gallic acid, chlorogenic acid, catechin, methyl gallate, syringic acid, rutin, ellagic acid, coumaric acid, vanillin, ferulic acid, naringenin, rosmarinic acid, daidzin, and quercetin.

Using UV-Vis spectroscopy, the characteristic absorption peaks of IPE were at 231, 271, 314 and 658 nm. The presence of these absorption bands is characteristic of alkaloids, flavonoids, and phenolic compounds (Karpagasundari et al., 2014; Mabasa et al., 2021; Patle et al., 2020).

The UV–VIS spectrum of the green-synthesized Se NPs revealed maximum absorption peaks at 233 and 277 nm corresponding to the surface plasmon resonance of Se NPs (Indhira et al., 2023). The presence of these peaks unequivocally confirmed the successful synthesis of Se NPs, consistent with previous studies (Lee et al., 2021; Wadhwani et al., 2017). The presence of a small peak at 277 nm could be due to IPE residues adsorbed onto the fabricated Se NPs surface. Regarding the FTIR spectrum of IPE, the detected peaks reveal the existence of phenolic compounds (Oliveira et al., 2016), alkaloids (Kalaichelvi and Dhivya, 2017), and terpenes (Mabasa et al., 2021; Were et al., 2015).

The functional groups detected by FTIR confirmed the stability of Se-NPs (Alagesan and Venugopal, 2019; Coccia et al., 2012; Kanchi and Khan, 2020). Moreover, there was red shifting or disappearing in vibration bands at 1074.85 and 1018.61 cm^{-1}, after Se NPs formation, suggesting that selenium ions may form complexes with C-N or C=N groups in the IPE (Yang et al., 2016). This result aligns with previously reported findings (Alagesan and Venugopal, 2019;

Chen et al., 2009; Jiang et al., 2022). However, some Bragg reflections with 2θ values at 11.6083 °, 22.122 ° and 34.4468 ° were observed in the XRD pattern of the Se NPs, confirming their nanocrystalline nature (Alagesan and Venugopal, 2019; Ramamurthy et al., 2013). The crystallite size of the Se NPs was calculated using the Scherrer equation with an average size of 68.43 nm, which demonstrates a high degree of consistency between the crystallite size values obtained from XRD and TEM.

The discrepancy between DLS and TEM measurements can be attributed to the influence of Brownian motion, which tends to overestimate particle size in DLS (Farkas and Kramar, 2021; Puri et al., 2023). In contrast, TEM provides a more accurate representation of the core particle size of NPs (Zhang et al., 2023). The Se NPs exhibited a high negative zeta potential of -26.42 ±0.351 mV, indicating strong stability as this negative charge, derived from oxidized polyphenols in the Se NPs, creates an electrostatic repulsion between particles, preventing aggregation (Sajadi et al. 2016). Additionally, the negative zeta potential of the Se NPs correlates with the negatively charged functional groups (hydroxyl and carboxyl groups) in IPE, facilitating their binding to the Se NPs surface (Mellinas, Jiménez, and Garrigós 2019; Puri et al. 2023).

The small size of the Se NPs revealed by TEM (70 ±10 nm) confirms the effecient wrapping and stabilizing potentials of IPE constituents (Eid et al., 2023). The EDX analysis reveals the elemental composition of the green-synthesized Se NPs. The presence of carbon and oxygen within the Se NPs provides evidence for the green synthesis approach, suggesting the involvement of organic compounds, such as capping agents or components forming Se NPs (Carmona et al., 2017).

In our study, the application of povidone-iodine and Se NPs to the infected wounds resulted in a noteworthy reduction (p<0.05) in the wound area and the CFU/g compared to the untreated positive control group at all postoperative time points (days 3–15). On the other hand, IPE exhibited significant effects starting from day 9. The histopathological evaluation provided additional confirmation of our results. Histological analysis of H&E-stained skin sections demonstrated normal epidermal and dermal architecture in the negative control group. In contrast, the positive control group exhibited epidermal loss accompanied by dense inflammatory infiltration and granulation tissue formation. Wounds treated with povidone-iodine showed complete re-epithelialization and the presence of abundant vascularized immature connective tissue. Treatment with IPE resulted in partial re-epithelialization with limited deposition of

connective tissue. Conversely, treatment with Se NPs achieved complete re-epithelialization and well-organized, mature vascularized connective tissue, indicating enhanced wound healing.

Our findings agree with previous investigations, that reported that histopathological evaluation of wound healing typically reveals inflammatory cell infiltration, granulation tissue formation, progressive collagen deposition, re-epithelialization, and tissue remodeling, reflecting the sequential and overlapping phases of healing (Diegelmann and Evans, 2004). These findings indicate that the Se NPs significantly enhanced wound healing, as evidenced by superior tissue regeneration and histological restoration compared to other treatments.

In our research, MDA and GSH levels were assessed in the wounded skin tissue to evaluate the oxidative stress. Injury induction led to a noteworthy escalation ($p<0.05$) in the MDA and a decline in the GSH compared to uninjured tissue from the negative control group, indicating elevated oxidative damage. Topical treatments significantly attenuated MDA levels and restored GSH concentrations relative to the positive control group. Notably, the Se NPs established superior efficacy in modulating oxidative stress markers compared to IPE. Previous studies revealed that reducing oxidative stress is crucial for effective wound healing (Kumandaş et al., 2020). Ferroptosis is a form of regulated cell death characterized by iron-dependent lipid peroxidation (Jia et al., 2023). It's essentially the opposite of what antioxidants do, as antioxidants prevent or reduce oxidation. Therefore, substances with antioxidant properties can potentially inhibit or mitigate ferroptosis (Ge et al., 2022). Ferroptosis may impair wound healing through several mechanisms. Excessive feroptotic cell death can delay tissue regeneration. Lipid peroxidation byproducts exacerbate inflammation, and prolonged inflammation is known to hinder repair processes (Hunt et al., 2024). Additionally, the oxidative stress intrinsic to ferroptosis can damage cellular components essential for healing.

Here, the topical treatment of infected wounds considerably elevated the levels of GPX4, ferritin, and HO-1 compared to the untreated positive control group. Notably, the Se NPs produced the highest increases in all three markers, indicating enhanced anti-inflammatory and anti-ferroptotic effects. GPX4 is an essential enzyme that safeguards cells against ferroptosis, a form of cell death induced by iron-dependent lipid peroxidation (Jiang and Bai, 2022). The elevation of GPX4 levels, particularly through the Se NPs treatment, likely inhibited ferroptosis within the wound environment. This inhibition is advantageous, as ferroptosis can exacerbate inflammation and impede the healing process (Liu et al., 2025). Ferritin serves as the primary protein for intracellular

iron storage. Elevated ferritin levels indicate an effort to sequester and regulate free iron (Zhao et al., 2017). Given that iron is a critical factor in ferroptosis, increased ferritin may act as a protective mechanism to limit iron availability for lipid peroxidation.

HO-1 is an enzyme that catalyzes the degradation of heme, releasing iron, carbon monoxide, and biliverdin. It is documented for its anti-inflammatory and antioxidant actions (Kumandaş et al., 2020). The upregulation of HO-1 suggests an active response to mitigate inflammation and oxidative stress in the wound.

Overall, the concurrent increase in GPX4, ferritin, and HO-1 exerted by the Se NPs fosters a protective environment in infected wounds by inhibiting ferroptosis and preventing uncontrolled cell death due to lipid peroxidation. Modulating iron metabolism thus reducing the availability of free iron to participate in deleterious reactions. Reducing Inflammation and oxidative stress and promoting a more balanced wound environment conducive to healing.

The expression of GPX4, PTGS2, and ACSL4 was evaluated in the infected wound tissue using qRT-PCR. The Se NPs significantly upregulated GPX4 and downregulated PTgs2 and Acsl4 compared to the untreated infected control. Notably, the Se NPs produced a distinct and significantly greater modulation of these ferroptosis-related genes compared to other treatment groups, indicating enhanced anti-ferroptosis activity.

Elevated expression of GPX4 is indicative of a reduction in ferroptosis. PTGS2, also known as cyclooxygenase-2 (COX-2), is an enzyme involved in prostaglandin synthesis and inflammation. Although it is not directly associated with ferroptosis, research suggests its upregulation in response to ferroptosis. Conversely, decreased expression may indicate reduced inflammation or a shift away from ferroptosis. The ACSL4 is an enzyme that facilitates the synthesis of long-chain fatty acids, which act as substrates for lipid peroxidation. Increased expression of ACSL4 suggests a heightened susceptibility to ferroptosis, whereas reduced expression implies a decrease in ferroptosis (Jia et al., 2023). Our findings indicate that Se NPs exerted a significantly greater influence on the gene modulation compared to other treatments. It enhanced GPX4 expression, strongly suggesting that the treatment actively suppresses ferroptosis. By augmenting GPX4 levels, cells are better equipped to detoxify lipid peroxides, thereby preventing cell death. The Se NPs significantly reduced PTGS2 expression, implying a potential reduction in the inflammation within the wound. Also, it significantly decreased the ACSL4 expression, suggesting a reduction in the cell's susceptibility to ferroptosis by limiting the availability of substrates for lipid

peroxidation. To the best of our knowledge, this study is the first to provide direct evidence linking the inhibition of ferroptosis to enhanced wound healing.

Immunohistochemical analysis was conducted to evaluate the expression of Nrf2, a main controller of the antioxidant response, and Ki-67, a marker of cell proliferation, in wounded skin. Topical application of the IPE caused a modest escalation in Nrf2 and a marked elevation in Ki-67 expression. Notably, treatment with the Se NPs has led to the highest expression levels of Nrf2 and Ki-67 among all groups, which has a great role in their wound healing potential.

The intersection of the bioactive compound targets with infected wound-related healing genes recognized 1226 shared targets. This overlap signifies that a significant portion of the bioactive compounds in the IPE are directly relevant to infected wound healing, offering targeted intervention points to mitigate disease progression.

The PPI network analysis elucidated hub genes, including TNF-α, IL-6, STAT3, and GAPDH, which possess a great role in the healing of infected wounds. This is due to their ability to control important functions such as the regulation of cell death and cell proliferation. Targeting these hub genes could be essential for developing new therapies. So, the modulation of these genes by the bioactive compounds present in IPE suggests potential therapeutic targets warranting further investigation.

Although we did not directly quantify TNF-α and IL-6 protein levels in our in vivo experiments, we have accumulated substantial indirect evidence from our biochemical analyses, gene expression studies, and histopathological assessments that robustly supports and corroborates the network pharmacology predictions concerning the suppression of these critical inflammatory pathways.

The pro-inflammatory cytokines TNF-α and IL-6 are recognized as master regulators that effectively induce the expression of prostaglandin-endoperoxide synthase 2 (PTGS2/COX-2), a crucial enzyme involved in the propagation of inflammation and pain. The marked downregulation of the PTGS2 gene expression observed in the Se NPs-treated group directly reflects the suppression of this anticipated TNF-α/IL-6 signaling pathway (Cui et al,2023)

The significant downregulation of the PTGS2 gene expression observed in the Se NPs-treated group is a direct functional outcome that aligns with the suppression of the predicted TNF-α/IL-6 signaling axis. A well-established antagonistic relationship exists between the NF-κB pathway, and TNF-α/IL-6, and the Nrf2 antioxidant pathway. The observed upregulation of Nrf2 and HO-1 in

the Se NP-treated group is well documented to suppress NF-κB activation, thereby attenuating downstream cytokines such as TNF-α and IL-6 (Alam et al., 2020; Sheng et al., 2024). The significant upregulation of Nrf2 and its downstream target, HO-1, by Se NPs provides a mechanistic explanation for the mitigation of the anticipated pro-inflammatory hub gene activity.

Tumor necrosis factor-alpha (TNF-α) has the capacity to modulate the expression of glutathione peroxidase 4 (GPX4), a critical regulator of ferroptosis. Elevated levels of TNF-α have been correlated with increased oxidative stress and lipid peroxidation, both of which are characteristic features of ferroptosis. Similarly, interleukin-6 (IL-6) has been implicated in the regulation of ferritin, an iron-binding protein that can attenuate ferroptosis by sequestering free iron (Li et al., 2023)

The molecular evidence is substantiated by histopathological observations, wherein treatment with Se NPs led to a significant reduction in polymorphonuclear cell infiltration—a characteristic histological indicator of TNF-α/IL-6-mediated inflammation—and facilitated the development of well-organized, mature connective tissue. This morphological evidence supports the notion of reduced local inflammation, aligning with the suppression of TNF-α and IL-6 activity (Impellizzeri et al., 2022)

Recent evidence indicates a significant correlation between ACSL4, TNF-α, and IL-6 in the regulation of inflammatory and reparative processes during wound healing. ACSL4, a pivotal enzyme in arachidonic acid metabolism, facilitates lipid peroxidation and ferroptotic cell death, thereby enhancing oxidative stress and inflammatory signaling. This activity can activate downstream pathways such as NF-κB, resulting in increased secretion of pro-inflammatory cytokines, including TNF-α and IL-6. In the initial stages of wound healing, elevated levels of TNF-α and IL-6 coordinate immune cell recruitment and activation, aiding in pathogen clearance and debris removal. However, sustained upregulation of ACSL4 is associated with persistent lipid peroxidation, which may drive prolonged TNF-α and IL-6 expression, contributing to chronic inflammation and impaired wound resolution. Conversely, controlled and transient expression of these mediators supports angiogenesis, fibroblast proliferation, and keratinocyte migration during the proliferative phase of repair. Thus, ACSL4, TNF-α, and IL-6 constitute an interconnected molecular network that governs the delicate balance between protective inflammation and pathological tissue damage in wound healing (Lam et al., 2024) Importantly, our study highlights

a significant correlation between ACSL4 and these inflammatory cytokines. ACSL4 modulates the inflammatory response by promoting TNF-α and IL-6 expression, suggesting a regulatory mechanism linking lipid metabolism with inflammatory signaling. This interplay is reflected experimentally by the downregulation of ACSL4 and inflammatory markers, alongside the upregulation of antioxidants (e.g., GPX4, HO-1, Nrf2), underscoring its role in balancing effective wound repair and inflammation resolution (Gao et al., 2024).

Future research could further investigate this relationship by directly assessing the expression or activity of TNF-α, IL-6, and other predicted inflammatory mediators in wound tissue samples.

Consequently, the integration of gene expression, protein-level, and histological data establishes a coherent "computational prediction → experimental validation" cycle, suggesting that the resolution of inflammation by Se NPs is facilitated through the modulation of these predicted hub genes and their associated pathways.

The KEGG pathway analysis revealed that lipid and atherosclerosis, microRNAs in cancer, and Kaposi sarcoma-associated herpesvirus (KSHV) infection were the three most prominent pathways enriched with bioactive compound target genes.

The interplay between lipids, atherosclerosis, and wound healing is intricate, with significant interconnections in inflammation and immune responses. Atherosclerosis is primarily a chronic inflammatory condition marked by lipid accumulation and inflammation within arterial walls. Lipids, particularly low-density lipoprotein (LDL) and its modified forms, accumulate in arterial walls, where they undergo oxidation and initiate inflammatory responses. Wound healing is a multifaceted process comprising inflammation, tissue formation, and remodeling. Lipids play a great role in this process as they are essential components of cellular membranes, signaling molecules, and energy sources. Research has demonstrated that lipids as phospholipids, sphingolipids, and ceramides I, influence inflammation, angiogenesis, and tissue regeneration, which are vital steps in wound healing (Choudhary et al., 2024). In other words, inflammation serves as a common link between lipids, atherosclerosis, and wound healing.

MicroRNAs (miRNAs) are small, non-coding RNA molecules that regulate gene expression at the post-transcriptional level, making significant contributions in various processes, including cancer development and wound healing. In the context of wound healing, miRNAs regulate crucial processes, as inflammation, proliferation, and tissue remodeling. They modulate gene expression

critical for maintaining the biology of wound sites and facilitate transitions necessary for healing (Mansour et al., 2025). Specifically, miRNAs have demonstrated a profound impact on chronic wounds, such as venous ulcers, where their dysregulation can impede the healing process. This regulatory role underscores their possible contribution as therapeutic targets for impaired wound healing. The interplay between miRNAs in cancer and wound healing suggests a possible bidirectional influence, wherein the oncogenic characteristics of miRNAs in cancer could alter normal wound repair processes, leading to chronic wound conditions or delayed healing. This connection may provide a pathway for future therapeutic strategies, where targeting miRNAs could simultaneously address tumor suppression and enhance wound healing processes.

The KEGG analysis has identified the 'Kaposi sarcoma-associated herpesvirus (KSHV) infection' pathway as significantly enriched. The significance of this pathway in wound healing is attributed to the fundamental host cellular processes that KSHV exploits. This virus strategically hijacks key signaling pathways—including NF-κB, MAPK, and those regulating apoptosis and angiogenesis—to promote cell survival, inflammation, and immune evasion (Komaki et al., 2024). Our network pharmacology results indicate that the bioactive compounds in IPE target these same host mechanisms. In the context of a dysregulated wound, this targeting likely results in a beneficial modulation of the healing process: mitigating excessive NF-κB-driven inflammation, protecting regenerative cells from ferroptosis, and promoting necessary angiogenic responses. This computational insight provides a novel systemic perspective that aligns with and supports our experimental findings of reduced inflammatory infiltrate, suppressed PTGS2 expression, and enhanced neovascularization and tissue maturation in Se NPs-treated wounds(Li et al., 2025).

Kaposi sarcoma-associated herpesvirus (KSHV) or human herpesvirus 8 (HHV-8) is involved in Kaposi's sarcoma (KS) pathogenesis and various other malignancies. KSHV infection can result in significant immune modulation, as the virus is capable of downregulating critical components of the adaptive immune response, including costimulatory receptors and proinflammatory cytokines, thereby evading host immune detection. This immunoreaction facilitates the persistence of KSHV infection, potentially affecting other immune-mediated processes, such as wound healing. Furthermore, KSHV has been demonstrated to have a connection with the cellular signaling pathways of cell proliferation and immune response suppression (Broussard and

Damania, 2020). These interactions may theoretically influence tissue regeneration and repair processes following tissue injury in wounds.

Conclusion

This study successfully demonstrated the green synthesis of Se NPs employing IPE, yielding stable, nanosized particles with predominantly spherical morphology. *In vitro* characterizations confirmed their formation, crystallinity, and stability. The presence of bioactive phytochemicals from the IPE played a vital pRT in capping and stabilizing the NPs, highlighting the potential of this eco-friendly method for producing biocompatible Se NPs suitable for future biomedical and industrial applications. Also, this study presents a comprehensive evaluation of the IPE green-synthesized Se NPs as a promising wound healing agent, emphasizing its multifaceted therapeutic potential. They exhibited antioxidant, anti-inflammatory, antibacterial, and anti-ferroptotic activities, providing novel mechanistic insights that link ferroptosis inhibition to enhanced wound repair. This multifaceted activity positions it as a novel wound therapeutic agent, particularly in managing infected wounds. In addition, using computational network pharmacology, the pertinent targets and pathways of the IPE in wound healing were revealed, in addition to their mechanism of action.

Reference

Akinniyi, G., Lee, J., Kim, H., Lee, J.-G., Yang, I.J.M.D., 2022. A medicinal halophyte Ipomoea pes-caprae (Linn.) R. Br.: A review of its botany, traditional uses, phytochemistry, and bioactivity. 20, 329.

Alam, M. B., Chowdhury, N. S., Sohrab, M. H., Rana, M. S., Lee, S.-H., & Hasan, C. M. (2020). Cerevisterol Alleviates Inflammation via Suppression of MAPK/NF-κB/AP-1 and Activation of the Nrf2/HO-1 Signaling Cascade. Biomolecules, 10(2), 199. https://doi.org/10.3390/biom10020199

Alagesan, V., Venugopal, S.J.B., 2019. Green synthesis of selenium nanoparticle using leaves extract of Withania somnifera and its biological applications and photocatalytic activities. 9, 105-116.

Altammar, K.A., 2023. A review on nanoparticles: characteristics, synthesis, applications, and challenges. Frontiers in microbiology 14, 1155622.

Broussard, G., Damania, B.J.F.i.i., 2020. KSHV: immune modulation and immunotherapy. 10, 3084.

Carmona, E.R., Benito, N., Plaza, T., Recio-Sánchez, G.J.G.C.L., Reviews, 2017. Green synthesis of silver nanoparticles by using leaf extracts from the endemic Buddleja globosa hope. 10, 250-256.

Chan, E.W.C., Baba, S., Chan, H.T., Kainuma, M., Tangah, J.J.I.J.o.N.P., Resources, 2016. Medicinal plants of sandy shores: A short review on Vitex trifolia L. and Ipomoea pes-caprae (L.) R. Br. 7, 107-115.

Chen, Z., Shen, Y., Xie, A., Zhu, J., Wu, Z., Huang, F.J.C.G., design, 2009. L-Cysteine-assisted controlled synthesis of selenium nanospheres and nanorods. 9, 1327-1333.

Choudhary, V., Choudhary, M., Bollag, W.B.J.I.j.o.m.s., 2024. Exploring skin wound healing models and the impact of natural lipids on the healing process. 25, 3790.
Coccia, F., Tonucci, L., Bosco, D., Bressan, M., d'Alessandro, N.J.G.C., 2012. One-pot synthesis of lignin-stabilised platinum and palladium nanoparticles and their catalytic behaviour in oxidation and reduction reactions. 14, 1073-1078.

Cui, J., Wang, Y., Tian, X., Miao, Y., Ma, L., Zhang, C., Xu, X., Wang, J., Fang, W., Zhang, X.J.A., signaling, r., 2023. LPCAT3 is transcriptionally regulated by YAP/ZEB/EP300 and collaborates with ACSL4 and YAP to determine ferroptosis sensitivity. 39, 491-511.

Diegelmann, R.F., Evans, M.C.J.F.b., 2004. Wound healing: an overview of acute, fibrotic and delayed healing. 9, 283-289.

Eid, A.M., Fouda, A., Hassan, S.E.-D., Hamza, M.F., Alharbi, N.K., Elkelish, A., Alharthi, A., Salem, W.M.J.C., 2023. Plant-based copper oxide nanoparticles; biosynthesis, characterization, antibacterial activity, tanning wastewater treatment, and heavy metals sorption. 13, 348.

Farkas, N., Kramar, J.A.J.J.o.N.R., 2021. Dynamic light scattering distributions by any means. 23, 120.
Forcina, G.C., Dixon, S.J.J.P., 2019. GPX4 at the crossroads of lipid homeostasis and ferroptosis. 19, 1800311.

Gao, Y., Huang, Y., Zhao, Y., & Hu, P. (2024). Cancer-associated fibroblast-secreted exosomal miR-454-3p inhibits lipid metabolism and ferroptosis in breast cancer by targeting ACSL4. Naunyn-Schmiedeberg's Archives of Pharmacology, 398(4), 3925–3937. https://doi.org/10.1007/s00210-024-03488-8

Ge, C., Zhang, S., Mu, H., Zheng, S., Tan, Z., Huang, X., Xu, C., Zou, J., Zhu, Y., Feng, D.J.F.i.c., biology, d., 2022. Emerging mechanisms and disease implications of ferroptosis: potential applications of natural products. 9, 774957.

Hunt, M., Torres, M., Bachar-Wikstrom, E., Wikstrom, J.D.J.C.b., 2024. Cellular and molecular roles of reactive oxygen species in wound healing. 7, 1534.

Impellizzeri, D., Fusco, R., Genovese, T., Cordaro, M., D'Amico, R., Trovato Salinaro, A., Ontario, M. L., Modafferi, S., Cuzzocrea, S., Di Paola, R., Calabrese, V., & Siracusa, R. (2022). Coriolus Versicolor Downregulates TLR4/NF-κB Signaling Cascade in Dinitrobenzenesulfonic Acid-Treated Mice: A Possible Mechanism for the Anti-Colitis Effect. Antioxidants, 11(2), 406. https://doi.org/10.3390/antiox11020406

Jia, B., Li, J., Song, Y., Luo, C.J.I.J.o.M.S., 2023. ACSL4-mediated ferroptosis and its potential role in central nervous system diseases and injuries. 24, 10021.

Jiang, H., Bai, X.J.F.i.P., 2022. Apolipoprotein AI mimetic peptides (ApoAI MP) improve oxidative stress and inflammatory responses in Parkinson's disease mice. 13, 966232.

Jiang, H., Wang, R., Zhou, F., Wu, Y., Li, S., Huo, G., Ye, J., Hua, C., Wang, Z.J.I.J.o.B.M., 2022. Preparation, physicochemical characterization, and cytotoxicity of selenium nanoparticles stabilized by Oudemansiella raphanipies polysaccharide. 211, 35-46.

Kalaichelvi, K., Dhivya, S.J.I.J.o.H.M., 2017. Screening of phytoconstituents, UV-VIS Spectrum and FTIR analysis of Micrococca mercurialis (L.) Benth. 5, 40-44.

Kamal, A.M., Shakour, Z.T.A., All, S., Sleem, A., Haggag, E.G.J.I.J.o.P., Research, P., 2017. Phytochemical and biological investigation of Ipomoea carnea Jacq. grown in Egypt. 9, 266-281.

Kanchi, S., Khan, A.J.B.R.A.C., 2020. Biogenic synthesis of selenium nanoparticles with edible mushroom extract: Evaluation of cytotoxicity on prostate cancer cell lines and their antioxidant, and antibacterial activity. 10, 6629-6639.

Karpagasundari, C., Kulothungan, S.J.J.o.P., Phytochemistry, 2014. Analysis of bioactive compounds in Physalis minima leaves using GC MS, HPLC, UV-VIS and FTIR techniques. 3, 196-201.

Komaki, S., Inagaki, T., Kumar, A., & Izumiya, Y. (2024). The Role of vIL-6 in KSHV-Mediated Immune Evasion and Tumorigenesis. Viruses, 16(12), 1900. https://doi.org/10.3390/v16121900

Kumandaş, A., Karsli, B., Kürüm, A., Çinar, M., 2020. Comparison of the effects of zinc-silver cream and Nigella sativa oil on wound healing and oxidative stress in the wound model in rats.

Lam, I.-H., Chan, C.-I., Han, M., Li, L., & Yu, H.-H. (2024). ACSL4 mediates inflammatory bowel disease and contributes to LPS-induced intestinal epithelial cell dysfunction by activating ferroptosis and inflammation. Open Medicine (Warsaw, Poland), 19(1). https://doi.org/10.1515/med-2024-0993

Lee, S.-C., Lee, N.-H., Patel, K.D., Jang, T.-S., Knowles, J.C., Kim, H.-W., Lee, H.-H., Lee, J.-H.J.N., 2021. The effect of selenium nanoparticles on the osteogenic differentiation of MC3T3-E1 cells. 11, 557.

Li, J., Chen, J., Kirsner, R.J.C.i.d., 2007. Pathophysiology of acute wound healing. 25, 9-18.

Li, Y., Zhang, L., & Dong, R. (2023). Research Progress in Regulation of Ferroptosis by Epigallocatechin-3-gallate in Tumor Cells. Letters in Drug Design & Discovery, 20(12), 1877–1883. https://doi.org/10.2174/1570180819666220819150351

Li, Z., Cao, Y., Li, H., Le, S., & Yin, L. (2025). Network Pharmacology, Molecular Docking Analysis and Experiment Validations on Molecular Targets and Mechanisms of the Dispel-Scar Ointment in Scar Treatment. Combinatorial Chemistry & High Throughput Screening, 28(13), 2318–2338. https://doi.org/10.2174/0113862073335953240820075044

Liu, Y., Guan, L., Yang, D., Luo, H., Zhang, H.J.F.c., 2025. Investigating the synergistic antibacterial effects of chlorogenic and p-coumaric acids on Shigella dysenteriae. 462, 141011.

Mabasa, X., Mathomu, L., Madala, N., Musie, E., Sigidi, M.J.B.R.I., 2021. Molecular Spectroscopic (FTIR and UV-Vis) and Hyphenated Chromatographic (UHPLC-qTOF-MS) Analysis and In Vitro Bioactivities of the Momordica balsamina Leaf Extract. 2021, 2854217.

Mansour, R.M., Mageed, S.S.A., Awad, F.A., Sadek, M.M., Adel, S.A., Ashraf, A., Alam-Eldein, K.M., Ahmed, N.E., Abdelaziz, R.Y., Tolba, E.F.J.F., Genomics, I., 2025. miRNAs and their multifaceted role in cutaneous wound healing. 25, 33.

Marles, R.J., Barrett, M.L., Barnes, J., Chavez, M.L., Gardiner, P., Ko, R., Mahady, G.B., Dog, T.L., Sarma, N.D., Giancaspro, G.I.J.C.r.i.f.s., nutrition, 2011. United States pharmacopeia safety evaluation of Spirulina. 51, 593-604.

Negm, W.A., El-Kadem, A.H., Elekhnawy, E., Attallah, N.G., Al-Hamoud, G.A., El-Masry, T.A., Zayed, A.J.P., 2022. Wound-healing potential of rhoifolin-rich fraction isolated from Sanguisorba officinalis roots supported by enhancing re-epithelization, angiogenesis, anti-inflammatory, and antimicrobial effects. 15, 178.

Oliveira, R.N., Mancini, M.C., Oliveira, F.C.S.d., Passos, T.M., Quilty, B., Thiré, R.M.d.S.M., McGuinness, G.B.J.M., 2016. FTIR analysis and quantification of phenols and flavonoids of five commercially available plants extracts used in wound healing. 21, 767-779.

Patle, T.K., Shrivas, K., Kurrey, R., Upadhyay, S., Jangde, R., Chauhan, R.J.S.A.P.A.M., Spectroscopy, B., 2020. Phytochemical screening and determination of phenolics and flavonoids in Dillenia pentagyna using UV–vis and FTIR spectroscopy. 242, 118717.

Perumal, S., Gopal Samy, M.V., Subramanian, D.J.B., Engineering, B., 2021. Selenium nanoparticle synthesis from endangered medicinal herb (Enicostema axillare). 44, 1853-1863.

Puri, A., Mohite, P., Patil, S., Chidrawar, V.R., Ushir, Y.V., Dodiya, R., Singh, S.J.F.i.C., 2023. Facile green synthesis and characterization of Terminalia arjuna bark phenolic–selenium nanogel: a biocompatible and green nano-biomaterial for multifaceted biological applications. 11, 1273360.

Ramamurthy, C., Sampath, K., Arunkumar, P., Kumar, M.S., Sujatha, V., Premkumar, K., Thirunavukkarasu, C.J.B., engineering, b., 2013. Green synthesis and characterization of selenium nanoparticles and its augmented cytotoxicity with doxorubicin on cancer cells. 36, 1131-1139.

Sheng, W., Yue, Y., Qi, T., Qin, H., Liu, P., Wang, D., Zeng, H., & Yu, F. (2024). The Multifaceted Protective Role of Nuclear Factor Erythroid 2-Related Factor 2 in Osteoarthritis: Regulation of Oxidative Stress and Inflammation. Journal of Inflammation Research, 17, 6619–6633. https://doi.org/10.2147/jir.s479186

Sultana, T., Islam, S., Azad, M.A.K., Akanda, M.J.H., Rahman, A., Rahman, M.S.J.F., 2024. Phytochemical Profiling and Antimicrobial Properties of Various Sweet Potato (Ipomoea batatas L.) Leaves Assessed by RP-HPLC-DAD. 13, 2787.

Wadhwani, S.A., Gorain, M., Banerjee, P., Shedbalkar, U.U., Singh, R., Kundu, G.C., Chopade, B.A.J.I.j.o.n., 2017. Green synthesis of selenium nanoparticles using Acinetobacter sp. SW30: optimization, characterization and its anticancer activity in breast cancer cells. 6841-6855.

Were, P., Waudo, W., Ozwara, H., Kutima, H.J.I.J.o.P., Research, P., 2015. Phytochemical analysis of warburgia ugandensis sprague using fourier transform infra-red (FT-IR) spectroscopy. 7, 201-205.

Xavier-Santos, J.B., Passos, J.G.R., Gomes, J.A.S., Cruz, J.V.C., Alves, J.S.F., Garcia, V.B., da Silva, R.M., Lopes, N.P., Araujo-Junior, R.F., Zucolotto, S.M.J.B., Pharmacotherapy, 2022. Topical gel containing phenolic-rich extract from Ipomoea pes-capre leaf (Convolvulaceae) has anti-inflammatory, wound healing, and antiophidic properties. 149, 112921.

Yang, H., Ren, Y.-y., Wang, T., Wang, C.J.R.i.p., 2016. Preparation and antibacterial activities of Ag/Ag+/Ag3+ nanoparticle composites made by pomegranate (Punica granatum) rind extract. 6, 299-304.

Zhang, S., Wang, C.J.M., Protocols, 2023. Precise analysis of nanoparticle size distribution in TEM image. 6, 63.

Zhao, H., Eguchi, S., Alam, A., Ma, D., 2017. The role of nuclear factor-erythroid 2 related factor 2 (Nrf-2) in the protection against lung injury. American Journal of Physiology-Lung Cellular & Molecular Physiology 312, L155-L162.